CHAPTER 3

Application of Radiogenic Isotopes in Geosciences: Overview and Perspectives

SVETLANA TESSALINA,*[a] FRED JOURDAN,[a] LAURIE NUNES,[a] ALLEN KENNEDY,[a] STEVEN DENYSZYN,[b] IGOR PUCHTEL,[c] MATHIEU TOUBOUL,[c] ROBERT CREASER,[d] MAUD BOYET,[e] ELENA BELOUSOVA[f] AND ANNE TRINQUIER[g]

[a] John de Laeter Centre for Mass Spectrometry, Curtin University, Perth, WA, Australia; [b] School of Earth and Environment, University of Bergen, The University of Western Australia, Australia; [c] Department of Geology, University of Maryland, 237 Regents Drive, College Park, MD 20742, USA; [d] Department of Earth & Atmospheric Sciences, University of Alberta, 126 Earth Sciences Building, Edmonton, Alberta, Canada; [e] Laboratoire Magmas et Volcans, Université Blaise Pascal, CNRS UMR 6524, 5 rue Kessler, 63038, Clermont-Ferrand, France; [f] Macquarie University, North Ryde, NSW, Australia; [g] Thermo Fisher Scientific, Hanna-Kunath-Str. 11, 28199, Bremen, Germany
*Email: Svetlana.Tessalina@curtin.edu.au

3.1 Introduction

Isotope geology is an integral part of the earth sciences, but its development would be impossible without the concepts of nuclear physics and chemical methods. The invention of the first mass spectrometer at the beginning of the 20th century made it possible to measure of the isotopic compositions of

RSC Detection Science Series No. 4
Principles and Practice of Analytical Techniques in Geosciences
Edited by Kliti Grice

Published by the Royal Society of Chemistry, www.rsc.org

the chemical elements that make up natural systems. Based on these measurements, the nuclear physics principle of radioactive decay enabled the direct age determination of rocks and minerals, which transformed geology into a quantitative science. Nowadays isotope geology addresses several fundamental questions of earth and planetary sciences, from astrophysics, the Earth's structures and internal dynamics to applied studies of the formation of mineral and oil deposits. The concept of isotopic tracers has allowed scientists to address the problems of environmental studies, erosion, and the transport of materials. This chapter brings together the recent advances in the field of isotope geology, but it is not meant to replace existing texts[1–3] covering basic notions and techniques.

3.2 Principles of Radioactive Decay

Some natural elements are unstable (see Table 3.1) and can transform spontaneously, by liberation of one or more particles and types of radiation. The principles of radioactive decay are described in detail elsewhere[1–4] and are only briefly summarised here.

A 'parent' element P (*e.g.* ^{187}Re) can decay to the 'daughter' element D (here ^{187}Os). During a unit of time, each atom of P has the same probability to decay. The number of disintegrations in time, $-\mathrm{P}/\mathrm{d}t$ (the minus indicates the decrease) is a product of this probability by the number of atoms in the system. The law of radioactive decay is expressed in the following manner (*Eqn* 3.1, Table 3.2). For any particular element, it is always the same fraction of parent element P that decays during a unit of time. This is expressed by equation 3.1 and can be rewritten as equation 3.1a, where λ is a constant of radioactive decay which is expressed in units inverse to the time:

$$\frac{\mathrm{dP}}{\mathrm{d}t} = -\lambda \mathrm{P} \tag{3.1}$$

$$\frac{\mathrm{dP}}{\mathrm{P}} = -\lambda \mathrm{d}t \tag{3.1a}$$

Table 3.1 Examples of radiogenic/radioactive isotopes.

H																	He
Li	***Be***		Re	Radioactive (P)				Os	Radiogenic (D)			B	***C***	N	O	F	Ne
Na	***Mg***											***Al***	Si	P	S	***Cl***	Ar
K	Ca	Sc	Ti	V	***Cr***	***Mn***	Fe	Co	Ni	Cu	Zn	Ga	Ge	As	Se	Br	Kr
Rb	Sr	Y	Zr	Nb	Mo	*Tc*	Ru	Rh	Pd	Ag	Cd	In	Sn	Sb	Te	I	Xe
Cs	Ba	Lu	Hf	Ta	W	Re	Os	Ir	Pt	Au	Hg	Tl	**Pb**	**Bi**	**Po**	**At**	**Rn**
Fr	**Ra**	*Lr*	*Rf*	*Db*	*Sg*	*Bh*	*Hs*	*Mt*	*Uun*	*Uuu*	*Uub*		*Uuq*				

La	Ce	Pr	Nd	*Pm*	Sm	Eu	Gd	Tb	Dy	Ho	Er	Tm	Yb
Ac	**Th**	**Pa**	**U**	*Np*	*Pu*	*Am*	*Cm*	*Bk*	*Cf*	*Es*	*Fm*	*Md*	*No*

C Cosmogenic nucleides **U** U-series (all radioactive) *Es* Not present on Earth

This equation may be integrated between time 0 and time t to give equation 3.2:

$$P(t) = P(0)e^{-\lambda t} \tag{3.2}$$

Most commonly we use T instead of λ, which is the time period during which element P(0) decays by half, otherwise known as the half-life. The relationship between λ and T can be established using the definition in equation 3.3. Applying equation 3.2 to the period T, an equation for time can be obtained (equation 3.4). This equation means that after 10 units of time, P(t) is decreased by a factor of approximately 1024 (2^{10}).

$$\frac{P(T)}{P(0)} = \frac{1}{2} \tag{3.3}$$

$$T = \frac{\ln(2)}{\lambda} \tag{3.4}$$

The number of daughter element (D) atoms freshly formed is equal to the number of decayed atoms of the parent element, as described in equation 3.5. The total number at time t, D(t), is equal to the initial number of D(0), already present in the system, plus the number of decayed parent isotopes (see equation 3.6). Using equation 3.2, we obtain equation 3.7, which is known as a practical expression of the radioactive decay law. It can be used in practice because, in general, P(t) is the actual value measured using the mass spectrometer, even if P(0) is unknown.

$$dF + dP = 0 \tag{3.5}$$

$$F(t) = F(0) + [P(0) - P(t)] \tag{3.6}$$

$$D(t) = D(0) + P(t)[e^{\lambda t} - 1] \tag{3.7}$$

This radioactive decay law may be used to date the systems containing the isotopes (rocks, minerals, *etc.*) using the following assumption: if we can estimate the variation of quantity of daughter element since the system's formation, we can calculate the age of this system.

Several types of radioactive decay have been recognised (Table 3.2).

3.3 Mass Spectrometry

3.3.1 General Principles

Ion source mass spectrometry using mass-to-charge separation of ionic species in a magnetic field was the outcome of pioneering work by Thomson,[5] Dempster,[6] Aston,[7] Bainbridge and Jordan,[8] and Nier.[9]

The aim of mass spectrometry is to disperse ions of differing masses and focus them onto a collection/detector system. This is achieved by accelerating an ion beam, containing ions of mass m with a velocity $\boldsymbol{v}$ and a charge

Table 3.2 Types of radioactive decay.

Type of decay	Decay equation	Example of isotope systematics
Alpha decay (α)	${}^{A}_{Z}A \rightarrow {}^{A-4}_{Z-2}B + {}^{4}_{2}He$	${}^{147}\mathrm{Sm} \rightarrow {}^{143}\mathrm{Nd} + {}^{4}_{2}He$
Beta-minus decay (β^-)	${}^{A}_{Z}A \rightarrow {}^{A}_{Z-1}B + e + \overline{\nu}$, or $n \rightarrow \mathrm{p} + \beta + \overline{\nu}$	${}^{87}\mathrm{Rb} \rightarrow {}^{87}\mathrm{Sr} + \beta + \overline{\nu}$
Beta-plus decay (β^+)	${}^{A}_{Z}A \rightarrow {}^{A}_{Z-1}B + e^+ + \nu$	${}^{187}\mathrm{Re} \rightarrow {}^{187}\mathrm{Os} + \mathrm{e}^+ + \nu$
Electron capture	${}^{A}_{Z}A + e^- \rightarrow {}^{A}_{Z-1}B + \nu$, or $p + e \rightarrow \mathrm{n} + \nu$	${}^{40}\mathrm{K} + \mathrm{e}^- \rightarrow {}^{40}\mathrm{Ar} + \nu$
Gamma-decay (γ)	${}^{A}_{Z}A \rightarrow {}^{A}_{Z}B + \gamma$	${}^{3}\mathrm{He} \rightarrow {}^{3}\mathrm{He} + \gamma$
Spontaneous fission	Fission is a chain reaction caused by neutrons when they have sufficient energy	$\mathrm{U} \rightarrow \mathrm{Kr} + \mathrm{Xe}$

n, neutron; p, proton; e, electron; ν, neutrino; $\bar{\nu}$, antineutrino; β, beta particle (high-speed electron or positron); γ - photon; A, neutron number; Z, proton number.
After Allègre.[2]

state q, through a potential difference V and then through a uniform magnetic field B. The kinetic energy, KE, acquired by each ion can be expressed as described in equation 3.8. If the velocity vector of the charged particle is perpendicular to the uniform magnetic field vector, the particle will move in a circular path of radius of curvature r, with radial and centripetal forces F given by equations 3.9 and 3.10 respectively.

$$KE = \frac{1}{2}m\boldsymbol{v}^2 = qV \tag{3.8}$$

$$\boldsymbol{F} = q\boldsymbol{v}\boldsymbol{B} \tag{3.9}$$

$$\boldsymbol{F} = \frac{m\boldsymbol{v}^2}{r} \tag{3.10}$$

By equating 3.9 and 3.10, the velocity vector v of a charged particle of mass m can be expressed as equation 3.11. If 3.11 is substituted into 3.8, we obtain equation 3.12. Therefore the radius of curvature of each ion of mass m can be written as described in equation 3.13.

$$q\boldsymbol{v}\boldsymbol{B} = \frac{m\boldsymbol{v}^2}{r} \rightarrow \boldsymbol{v} = \frac{q\boldsymbol{B}r}{m} \tag{3.11}$$

$$\frac{m}{q} = \frac{r^2\boldsymbol{B}^2}{2V} \tag{3.12}$$

$$r = \frac{1}{\boldsymbol{B}}\sqrt{\left(\frac{m}{q}\right) \times 2V} \tag{3.13}$$

Heavier ion beams will therefore have a larger radius of deflection in relation to lighter ion beams, resulting in a dispersion of the composite beam.[10] However, given the inherent angular spread of the composite ion beam (in the horizontal plane), aberrations in the dispersed beam will produce slightly different radial paths for ions with the same mass, thereby leading to an unfocused ion beam at the detector. Therefore, to minimise these aberrations and maximise dispersion, a magnetic sector field is used such that dispersed ion beams come into focus outside the magnetic field. In addition to this dispersion and focusing of ion beams moving in the horizontal plane, the magnetic sector field has the property that it can focus the ion beam in the *z*-plane given the inherent fringing property of the magnetic field, thereby vertically deflecting diverging ion beams.[11] This arrangement is referred to as 'stigmatic double focusing' where the focusing action will occur when $\Phi = 90^\circ$; $L' = L'' = 2r$; $\varepsilon_1 = \varepsilon_2 = 26.5^\circ$; $\Omega = 37^\circ$. A schematic of this arrangement is shown in Figure 3.1.

Dispersed ions that emerge from the magnetic sector field are then collected *via* a detection/collection system outside the magnetic field. The collection system will either be multi-collection, whereby different mass ion beams are collected simultaneously, or peak jumping, whereby the ion beam of a single mass is collected at a time. For the latter, the magnetic field strength is varied to change the radii of the path of the ions through the magnet so that ions of different m/q ratios can be directed into a detector slit in succession.

Mass spectrometers operate in a high vacuum system in order to prevent collisions of ions with residual gas molecules during the flight from the ion source to the detector. The vacuum should be such that the mean free path of the ion is orders of magnitude longer than the distance from the ion source to the detector.

In thermal ionisation mass spectrometry (TIMS), a charged ion beam is generated when a filament assembly, containing a suitable sample deposit, is heated under vacuum conditions. The probability that an atom is ionised

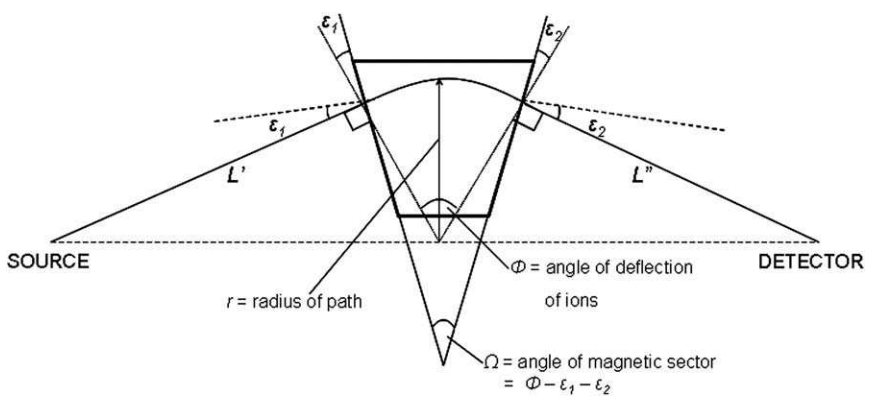

Figure 3.1 General schematic of a mass spectrometer magnetic sector arrangement. Reproduced with permission from Cross.[11]

and ejected with low energy from the filament surface can be determined using the Saha–Langmuir equation (equation 3.8), which represents the ionisation efficiency of positively charged ions in a thermal ionisation source (equation 3.14).

$$E = \frac{N^+}{N^o} A e^{[(\phi - I)/kT]} \tag{3.14}$$

where N^+ is the number of positively charged ions leaving the filament, N^o is the number of neutral atoms, A is a constant, ϕ is the work function of the filament, I is the ionisation potential of the ionised particles, k is the Boltzmann constant, and T is the temperature. The degree of ionisation (N^+/N^o) is therefore dependent upon the ionisation potential of the element I: if this is low, ($\phi - I$) is positive and the source is very efficient. For elements with a high ionisation potential, *i.e.* ($\phi - I$) is negative, then the maximum efficiency is obtained when T is as large as possible.

Significant proportions of present-day mass spectrometers employ thermal ionisation or inductively coupled plasma ionisation techniques.

3.3.2 Thermal Ionisation and Noble Gas Mass Spectrometry

Thermal ionisation is achieved by passing a current through a refractory metal filament on which the sample is deposited.[12] This versatile and robust method has been extensively used in multiple scientific applications. because of the high ionisation potentials of some elements, a number of strategies have been developed to enhance ionisation efficiency, either by addition of colloidal solutions, the use of multiple filament assemblies, or negative ion analysis. Thermal ionisation efficiencies range from 0.001% to 40% of the sample load. Memory effects from previous samples are negligible and isobaric interferences are mainly a function of analyte purity. Once ionised, the sample is accelerated in an electrical potential and the resulting ion beams are deflected in a magnetic field according to the mass-to-charge ratios. To avoid collision with gas molecules, the ion beams travel in a high vacuum. The relative isotopic abundance is measured by the comparison of ion beam intensities. The collectors are either Faraday cups, or, for low-intensity beams, ion counters. Faraday cups convert the incident charges into a current, which in turn is amplified. Low-intensity ion beams generate electric currents in ion counters through emission of secondary electrons, which are subsequently amplified. TIMS analyses introduce a mass-dependent analytical bias (fractionation), which occurs upon evaporation and evolves with the consumption of the sample. The magnitude of fractionation is of the order of 1% by mass unit for light elements (*e.g.* lithium), and 0.1% by mass unit for heavy elements (*e.g.* uranium). The fractionation can be accurately modelled by the Rayleigh diffusion law and can be corrected for by internal normalisation, double spike techniques, or total evaporation. The magnitude of the mass-dependent fractionation in plasma source mass spectrometers is up to 10 times greater.

In its simplest form, a sample is dried on the filament surface of a single filament assembly as a solution of the chloride, nitrate, or oxide of the element concerned. In some cases, an ionisation enhancer is used to improve the ionisation efficiency on the filament.[13–15 and references therein] The sample is then carefully taken to dryness and the assembly is mounted into the mass spectrometer ion source. The filament is then heated under vacuum conditions leading to evaporation/vaporisation of the sample. Generated neutral atoms then interact with the hot surface of the filament material and may be positively ionised.

If the sample being analysed has a high ionisation potential, high temperatures are required in order to achieve sufficient ionisation efficiency. However, this may result in the filament melting and/or the sample evaporating before ionisation can occur. Therefore, two- and three-filament assemblies are used, allowing the heating of each filament in the assembly to be independently controlled. The two-filament assembly consists of an evaporation filament which the sample is mounted on to and evaporated at low temperature, and an ionisation filament which ionises evaporated neutral atoms and is maintained at a higher temperature. In the triple-filament arrangement, the sample is mounted on two side filaments, which, when heated, vaporise the sample; evaporated neutral atoms are then ionised by the central filament.[10,16]

Rhenium is often preferred as the filament material because of its high work function (4.98 eV) and high melting point (3180 K).[10] Other filament materials that are used are tantalum, tungsten, and platinum.

Noble gas mass spectrometers (*i.e.* for $^{40}Ar/^{39}Ar$ isotope measurement) follow the same general principle as TIMS, with the exception that a gaseous sample consisting of noble gases is purified in an extraction line and introduced directly into the ion source chamber. A tungsten coiled-wire filament continuously heated at high temperature emits electrons that are accelerated by electric potential. Electrons, with an initial energy of 50–100 eV and a small permanent magnet to increase the length of their trajectory through the gas, hit and ionise (single-charge) noble gas atoms. The ions are then accelerated through plates with a variable voltage of several thousand volts, whereas the electrons emitted from the filament are recovered by the electron trap.

3.3.3 Isotopic Dilution

In order to learn the particular elemental contents (*e.g.* osmium) of a sample with known isotopic ratios (measured using the mass spectrometer), the quantity of osmium isotopes must be known. TIMS instruments especially provide excellent measurements of isotopic ratios but signal levels depend poorly on the size of the loads. Isotope dilution is a way to measure contents very precisely using the measurements of isotopic ratios. Addition of a precise quantity of ^{190}Os, which is a stable osmium isotope, allows us to estimate the quantity of ^{188}Os by measuring the $^{190}Os/^{188}Os$ isotope ratio.

This addition of enriched isotope tracer is referred to as the isotopic dilution technique. In order to know the contents of other radiogenic isotopes we use the same technique, adding a precise amount of enriched stable isotope and measuring the isotopic ratios of the mixture. It is important to notice that the isotopic equilibrium should be achieved between the sample and spike.

The $^{190}Os/^{188}Os$ ratio of the mixture may be expressed as:

$$\left(\frac{^{190}Os}{^{188}Os}\right)_{mixture} = \frac{(^{190}Os)_{sample} + (^{190}Os)_{spike}}{(^{188}Os)_{sample} + (^{188}Os)_{spike}} = \frac{\left(\frac{^{190}Os}{^{188}Os}\right)_{spike} + \left(\frac{^{190}Os}{^{188}Os}\right)_{sample}\left[\frac{^{188}Os_{sample}}{^{188}Os_{spike}}\right]}{1 + \left[\frac{^{190}Os_{sample}}{^{190}Os_{spike}}\right]} \quad (3.15)$$

After dividing the top and bottom of this equation by ^{188}Os and other minor manipulations, we obtain for the ^{188}Os contents of the rock under study as:

$$^{188}Os_{sample} = {}^{188}Os_{spike}\left(\frac{^{190}Os}{^{188}Os}\right)_{spike} \frac{\left(\frac{^{190}Os}{^{188}Os}\right)_{spike} - \left(\frac{^{190}Os}{^{188}Os}\right)_{mixture}}{\left(\frac{^{190}Os}{^{188}Os}\right)_{mixture} - \left(\frac{^{190}Os}{^{188}Os}\right)_{sample}} \quad (3.16)$$

Using this equation with known ^{188}Os content of the spike and measuring the isotopic ratios of the mixture, the Os content of the studied sample can be calculated.

This method is applicable for a range of elements with several stable isotopes. Spikes are usually artificially enriched in one or more stable isotopes. The isotopic dilution method therefore has several advantages. First, highly accurate precision is attained after isotopic equilibrium with the sample is achieved, even if the chemistry does not yield a 100% score. Another advantage is the great precision in measuring very low-level trace elements due to the high precision of isotopic ratio measurements using mass spectrometry. The best results are achieved by calibrating each mass spectrometer against the international isotopic standards.

3.3.4 International Isotopic Standards

Each mass spectrometer has its own characteristics and it is quite difficult to get a precisely consistent isotopic ratio among many mass spectrometers from different manufacturers. A reference sample should be used to find the instrumental bias for an individual mass spectrometer. For example, for the isotopic composition of neodymium, the La Jolla neodymium standard prepared by Lugmair and Carlson[17] is mostly used to monitor the instrumental bias. The reference rock material with homogeneous contents and

isotopic ratios of elements of interest are also used to estimate the precision of techniques used, accuracy of spike calibration, and chemical preparation.

In what follows, several short and long-lived isotopic systems and their application in earth sciences are described in detail.

3.4 Short-Lived Isotopes

3.4.1 Extinct Radioactivity

An extinct radioactive decay system is one where the radioactive parent isotope may have been present at the time the solar system was formed, 4.56 billion years ago, but has now decayed to undetectable levels. Since the parent isotope is no longer present an absolute age cannot be determined and only a relative chronology can be obtained. A critical assumption of radiometric decay systems is that the parent and daughter elements were initially homogeneous in isotopic composition throughout the system under investigation. Also, the decay system must remain closed to loss or gain of the parent and daughter elements after formation. If these constraints hold, then the abundance of the daughter isotope, which changes rapidly over short time intervals in these systems, can be measured and used to calculate relative ages that have excellent temporal resolution. A large number of these systems have been studied in meteorites and this has produced a fine-scale chronology of early solar system processes that fractionate the parent–daughter ratios of each system before the parent isotope became extinct. Examples of extinct parent isotope–daughter isotope systems studied in meteorites are ^{10}Be–^{10}B, ^{26}Al–^{26}Mg, ^{41}Ca–^{41}K, ^{53}Mn–^{53}Cr, ^{60}Fe–^{60}Ni, ^{107}Pd–^{107}Ag, ^{129}I–^{129}Xe, ^{182}Hf–^{182}W, and ^{146}Sm–^{142}Nd (Table 3.3). These decay systems have half-lives ranging from 0.1 Ma for ^{10}Be to 68 Ma for ^{146}Sm. We describe some of these in more detail below.

3.4.2 ^{26}Al: Isotopic Anomalies in ^{26}Mg

Aluminium possesses a radioactive isotope ^{26}Al, with a short half-life of 0.72 Ma. More than 99% of the ^{26}Al will decay to produce ^{26}Mg in 5 million years, and therefore ^{26}Al rapidly becomes extinct. ^{26}Al was produced by pre-solar stellar nucleosynthesis and incorporated into the solar nebula just prior to condensation of CAI (refractory, high temperature, calcium–aluminium-rich inclusions found in chondritic meteorites), magnesium-rich chondrules, and fine matrix materials. Accretion of these components and dust from the nebula led to the formation of chondritic meteorites, and ultimately, the rocky planets of our solar system. Magnesium and aluminium are both abundant in the solar system; aluminium has one stable isotope, ^{27}Al, and magnesium has three, ^{24}Mg, ^{25}Mg, and ^{26}Mg in the following proportions: 79%, 10%, and 11%. In contrast, ^{26}Al is rare, as the ^{26}Al/^{27}Al ratio at the time of formation of the first solar system objects was measured to be $\sim 5.23 \times 10^{-5}$.[18–21] Hence, an excess of ^{26}Mg produced by radioactive decay of ^{26}Al is extremely difficult to identify in magnesium-bearing material.

Table 3.3 Summary of selected radiogenic systematics with their respective decay type and half-lives.

Isotopic system	Type of decay	Half-life
Short-lived isotope systematics		
^{10}Be–^{10}B	β^- : $^{10}\mathrm{Be} \rightarrow {}^{10}\mathrm{B} + \beta^-$	0.1 Ma
^{41}Ca–^{41}K	Electron capture: $^{41}\mathrm{Ca} + e^- \rightarrow {}^{41}\mathrm{K} + \nu$	0.1 Ma
^{26}Al–^{26}Mg	Electron capture: $^{26}\mathrm{Al} + e^- \rightarrow {}^{26}\mathrm{Mg} + \nu$ and β^+ : $^{26}\mathrm{Al} \rightarrow {}^{26}\mathrm{Mg} + e^+ + \nu$	0.7 Ma
^{60}Fe–^{60}Ni	*series of* β^- : $^{60}\mathrm{Fe} \rightarrow {}^{60}\mathrm{Co} + e + \overline{\nu} \rightarrow {}^{60}\mathrm{Ni} + e + \overline{\nu}$	1.5 Ma
^{53}Mn–^{53}Cr	Electron capture: $^{53}\mathrm{Mn} + e^- \rightarrow {}^{53}\mathrm{Kr} + \nu$	3.7 Ma
^{107}Pd–^{107}Ag	*Combined (electron capture + γ-rays):* $^{108}\mathrm{Pd} + e^- \rightarrow {}^{108}\mathrm{Ag} + \nu + \gamma$	6.5 Ma
^{182}Hf–^{182}W	β^- : $^{182}\mathrm{Hf} \rightarrow {}^{182}\mathrm{W} + \beta^-$	8.9 Ma
^{129}I–^{129}Xe	β^- : $^{129}\mathrm{I} \rightarrow {}^{129}\mathrm{Xe} + \beta^-$	17 Ma
^{146}Sm–^{142}Nd	α : $^{146}\mathrm{Sm} \rightarrow {}^{142}\mathrm{Nd} + {}^{4}_{2}\mathrm{He}$	68 Ma
Long-lived isotope systematics		
^{190}Pt–^{186}Os	α : $^{147}\mathrm{Sm} \rightarrow {}^{143}\mathrm{Nd} + {}^{4}_{2}\mathrm{He}$	469 Ga
^{147}Sm–^{143}Nd	α : $^{147}\mathrm{Sm} \rightarrow {}^{143}\mathrm{Nd} + {}^{4}_{2}\mathrm{He}$	106 Ga
^{87}Rb–^{87}Sr	β^- : $^{87}\mathrm{Rb} \rightarrow {}^{87}\mathrm{Sr} + \beta^-$	49 Ga
^{187}Re–^{187}Os	β^+ : $^{187}\mathrm{Re} \rightarrow {}^{187}\mathrm{Os} + e^+ + \nu$	42 Ga
^{176}Lu–^{177}Hf		37 Ga
^{40}K–^{40}Ar	Electron capture: $^{40}\mathrm{K} + e^- \rightarrow {}^{40}\mathrm{Ar} + \nu$	12 Ga
^{40}K–^{40}Ca	β^- : $^{40}\mathrm{K} \rightarrow {}^{40}\mathrm{Ca} + \beta^-$	1.4 Ga
U–Th–Pb systems (uranium series decay: α^+ spontaneous fusion)		
^{232}Th–^{208}Pb	$^{232}\mathrm{Th} \rightarrow {}^{208}\mathrm{Pb} + 6^{4}_{2}He + 4\beta^-$	14 Ga
^{235}U–^{207}Pb	$^{235}\mathrm{U} \rightarrow {}^{207}\mathrm{Pb} + 7^{4}_{2}He + 4\beta^-$	704 Ma
^{238}U–^{206}Pb	$^{238}\mathrm{U} \rightarrow {}^{206}\mathrm{Pb} + 8^{4}_{2}He + 6\beta^-$	4468 Ma

However, an understanding of the distribution of ^{26}Al is critical to models of planetary formation and solar system evolution. If accretion occurred shortly after formation of ^{26}Al, then the decay of ^{26}Al would produce sufficient heat to produce melting and igneous differentiation of planetary bodies.[22]

The first evidence of ^{26}Mg from decay of ^{26}Al was found in early-condensed aluminium-rich material that is virtually devoid of magnesium phases within CAI.[23,24] The presence of excess of ^{26}Mg shows these materials formed very early in the evolution of the solar system, less than a million years after nucleosynthesis of ^{26}Al and quite possibly within a 20 000 year time window.[18] Although finding evidence for decay of ^{26}Mg is extremely difficult in magnesium-rich materials, recent high-precision magnesium isotope analysis has shown the magnesium-rich phases in some chondrules did form with elevated ^{26}Al/^{27}Al ratios, with values up to $\sim 0.7 \times 10^{-5}$ and an initial ^{26}Mg/^{24}Mg ratio close to the measured initial solar system value,[19] suggesting they formed at a much earlier time than most chondrules. Other studies of magnesium-rich chondrules measure much lower initial ^{26}Al abundances, $\leq 1 \times 10^{-6}$, and this is consistent with the later formation of these chondrules.[19,25] A 1.2–4 Ma age difference between CAIs and chondrule formation is the conclusion of many ^{26}Al studies interpreted under the

assumption of an homogeneous distribution of ^{26}Al in the inner solar system.[19–21,26] Villeneuve *et al.*[19] also show there are a number of peaks in the distribution of ^{26}Al–^{26}Mg ages for chondrules from a single parent body, and this suggests that chondrule formation occurred in pulses over a period of several million years. The assumption of a solar nebula with a homogeneous initial magnesium isotope composition is incorrect, as there are numerous examples of low-level (100 ppm) heterogeneity of initial magnesium isotopic composition (*i.e.* variable $(\delta^{26}Mg^*)_0$) in high-precision studies.[22,27] However, this does not prevent the use of the ^{26}Al–^{26}Mg geochronometer, but simply restricts its use to the comparison of materials that are shown to have the same $(\delta^{26}Mg^*)_0$.

Magnesium isotopic compositions are typically expressed as isotopic ratios relative to a reference isotopic composition. The δ^{26}Mg notation gives the relative deviation, in parts per thousand (‰), of the ^{26}Mg/^{24}Mg ratio from the reference isotopic composition, typically an international reference material.

Figure 3.2 shows examples of ^{26}Al–^{26}Mg isochrons. If the data of Figure 3.2 is interpreted in a simple model where time zero equates to the homogenisation of the nebular source with $(^{26}Al/^{27}Al)_i = 5.23 \times 10^{-5}$ and $(\delta^{26}Mg^*)_i = -0.038‰$, the three isochrons show that crystallisation of the 3535–1 CAI, the 3665A CAI, and the Semarkona chondrule occurred at three different points in time during the evolution of the solar system, at ~0.05 Ma, 0.29 Ma, and 2.5 Ma, respectively, after time zero.

In summary, the ^{26}Al–^{26}Mg cosmochronometer, which is based on decay of an extinct isotope, allows us to precisely define relative time differences of approximately 10 000 years, 4.567 billion years ago, for materials with identical initial magnesium isotopic compositions, and this allows us to follow and understand the earliest history of the solar system in great detail.

3.4.3 ^{182}Hf–^{182}W Isotope System

3.4.3.1 Introduction

The short-lived ^{182}Hf–^{182}W isotopic system is characterised by a short half-life of 8.9 Ma,[28] which is well suited for timescales of the formation and earliest evolution of solar system objects. The main interest in the Hf–W system was initially related to its potential for dating core formation.[29–31] Hafnium and tungsten are both refractory elements and are presumed to occur in chondritic relative abundances in bulk planetary objects. Tungsten is a moderately siderophile element (MSE) and is largely, but not completely, drained into the metal during core segregation.[32,33] In contrast, hafnium is strictly lithophile and is completely retained in silicate portions of planetary bodies. Planetary cores, which contain virtually no hafnium and hence no radiogenic ^{182}W, have frozen the tungsten isotopic composition at the time of their formation. The tungsten isotopic compositions of magmatic iron meteorites[34–38] are close to the initial isotopic composition of chondrites

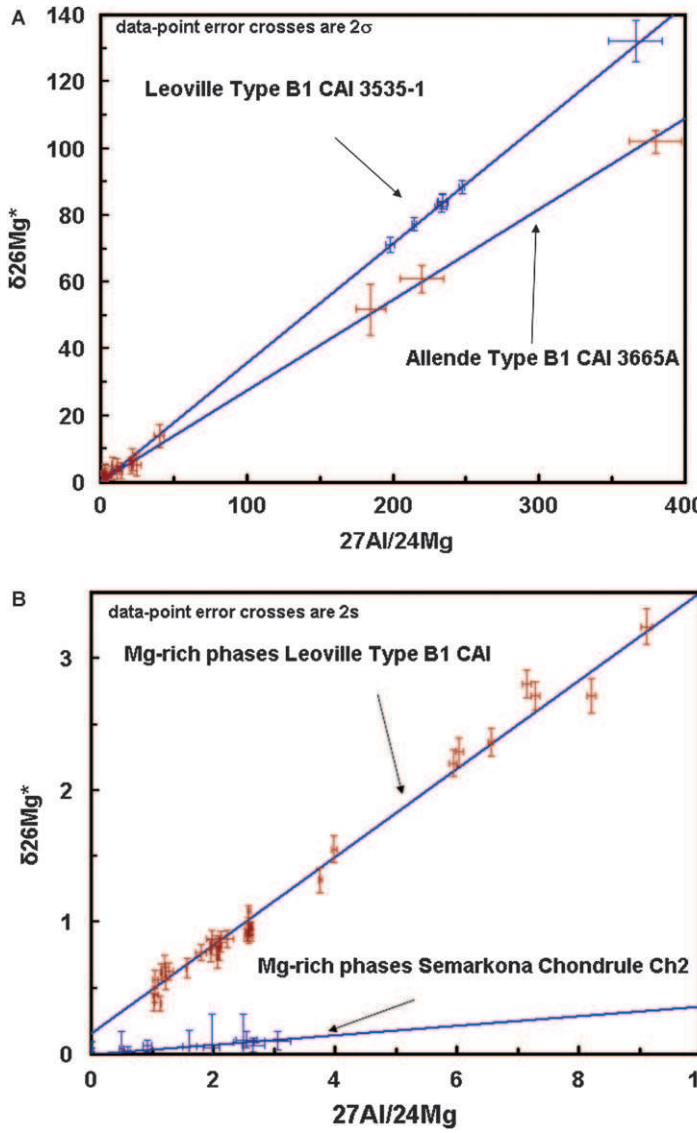

Figure 3.2 The ^{26}Al–^{26}Mg isochrones: (A) ^{26}Al–^{26}Mg isochrons measured in two type B1 CAI, 3535-1 from Leoville CV3 carbonaceous chondrite (Kita *et al.*[21]) and 3665A from the Allende CV3 carbonaceous chondrite (Kennedy *et al.*[27]). The 3535-1 isochron has an initial $(^{26}Al/^{27}Al)_0$ of $5.002 \pm 0.65 \times 10^{-5}$ and a $(\delta^{26}Mg^*)_0$ of 0.06 ± 0.08‰, while 3665A has $(^{26}Al/^{27}Al)_0$ of $3.95 \pm 4.2 \times 10^{-5}$ and a $(\delta^{26}Mg^*)_0$ of 0.44 ± 0.38‰. (B) ^{26}Al–^{26}Mg isochrons for magnesium-rich phases from the Leoville CV3 carbonaceous chondrite (Kita *et al.*[21]) and a chondrule (Ch2) from the Semarkona LL3 ordinary chondrite (Villeneuve[19]). The CAI isochron has an initial $(^{26}Al/^{27}Al)_0$ of $5.002 \pm 0.65 \times 10^{-5}$ and a $(\delta^{26}Mg^*)_0$ of 0.06 ± 0.08‰, while the chondrule isochron has a $(^{26}Al/^{27}Al)_0$ of $5.071 \pm 1.8 \times 10{-}^{6}$ and a $(\delta^{26}Mg^*)_0$ of -0.003 ± 0.01‰.

4568 Ga ago, as determined from hafnium–tungsten internal isochrons of CAI,[39,40] indicating core formation and hence accretion of some differentiated planetesimals less than 1 Ma after solar system formation.

3.4.3.2 Core Formation

Model ages of core formation can also be inferred using the tungsten isotope composition of silicate portions of planetary bodies. Terrestrial rocks[41–43] and Martian meteorites[39,44,45] have radiogenic $^{182}W/^{184}W$ ratios relative to bulk chondrites (Figure 3.3). The higher than chondritic $^{182}W/^{184}W$ ratios of the terrestrial and Martian mantles have been interpreted to reflect core segregation and generation of a highly suprachondritic hafnium/tungsten ratio in the silicate portion of terrestrial planets, while ^{182}Hf was still extant. Combined with current best estimates for the hafnium/tungsten ratio of bulk Martian[46] and terrestrial mantles,[47] these yield hafnium–tungsten model ages

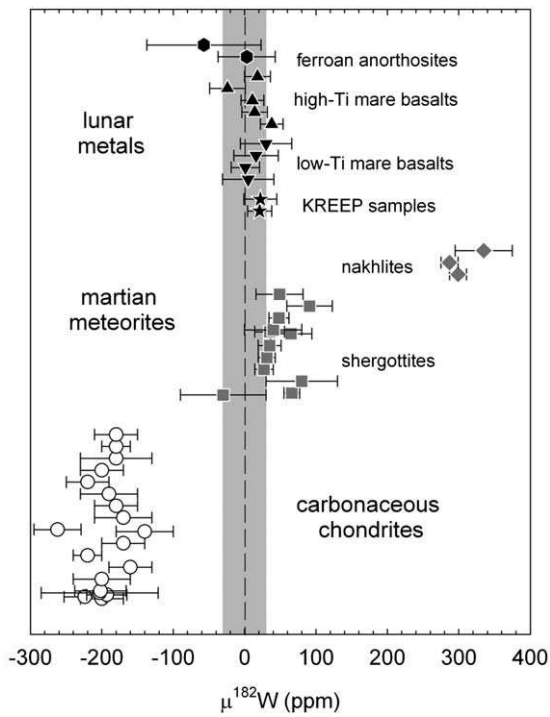

Figure 3.3 $^{182}W/^{184}W$ ratios of carbonaceaous chondrites (open circles), Martian meteorites (grey symbols) and lunar samples (closed symbols), expressed in $\mu^{182}W$ notation, which corresponds to parts per million deviation of the isotpic ratio of the sample from terrestrial standards. Data are from Yin *et al.*,[43] Kleine *et al.*,[39] Foley *et al.*,[45] and Touboul *et al.*[48,49] Grey box indicates the 2δ external reproducibility classically reached during these studies ($\sim \pm 30$ ppm).

of ~2 and ~30 Ma for core formation on Mars and Earth, respectively, assuming these processes occur as single instantaneous events. This assumption might be justified for Mars, which likely corresponds to a planetary stranded embryo, but it is difficult to reconcile with the occurrence of giant impacts which characterised subsequent accretion of larger planets such as Earth. The calculated hafnium–tungsten model age of the Earth's core is very sensitive to the timing of these large collisions and to the degree of equilibration of impactor cores with the proto-Earth mantle and range from ~30 Ma to more than 100 Ma after solar system formation. Therefore, hafnium–tungsten systematics of the Earth's mantle does not provide a unique time constraint for the formation of the Earth. Nevertheless, the identical $^{182}W/^{184}W$ ratios of the lunar and terrestrial mantles[48,49] suggest that the giant Moon-forming impact and the termination of Earth's core formation occurred after extinction of ^{182}Hf (*i.e.* more than ~50 Ma after CAIs). Furthermore, this isotopic similarity requires that the Moon consists predominantly of terrestrial material, consistent with the most recent dynamical simulations of the Moon-forming giant impact.[50,51] Alternatively, tungsten isotopes might have been equilibrated between the proto-lunar disk and Earth's magma ocean, as proposed for oxygen isotopes by Pahlevan and Stevenson.[52]

3.4.3.3 Early Mantle Differentiation

In addition to core formation, the ^{182}Hf–^{182}W system can also be used for exploring early mantle differentiation. Tungsten is one of the most incompatible elements, similar to thorium and uranium. Hafnium is also an incompatible element; however, relative to tungsten, it is preferentially incorporated in minerals such as clinopyroxene, ilmenite, garnet, and magnesium perovskite.[53,54] Crystallisation of these phases (*e.g.* during solidification of a magma ocean) or their partial melting (*e.g.* during crustal extraction) can result in the production of mantle reservoirs with variable hafnium/tungsten ratios. If these reservoirs formed within the lifetime of ^{182}Hf (less than ~60 Ma after solar system formation), differences in their Hf/W hafnium/tungsten ratio would translate into variations of their $^{182}W/^{184}W$ ratio. ^{182}W heterogeneities are present within the Martian mantle, as revealed by the difference of tungsten isotopic composition between shergottites and nakhlites (Figure 3.3).[39,44,45] This indicates a solidification of a Martian magma ocean during the effective lifetime of ^{182}Hf, most likely ~40 Ma after the start of the solar system. In contrast to Mars, there is no $^{182}W/^{184}W$ variation in the lunar mantle,[48,49] indicating magma ocean solidification later than ~60 Ma, consistent with the ~150 Ma timescale derived from ^{146}Sm–^{142}Nd chronometry[55] and the young age of 4.360 Ga for the ferroan anorthosite 60025.[56]

The possibility of identifying early magmatic processes within the Earth's mantle has led to intensive tungsten isotopic analysis of diverse terrestrial materials. Until recently these studies have reported no resolved ^{182}W isotopic heterogeneities among terrestrial rocks,[57–59] but recent improvements in precision of tungsten isotope measurements [60] have enabled evidence for

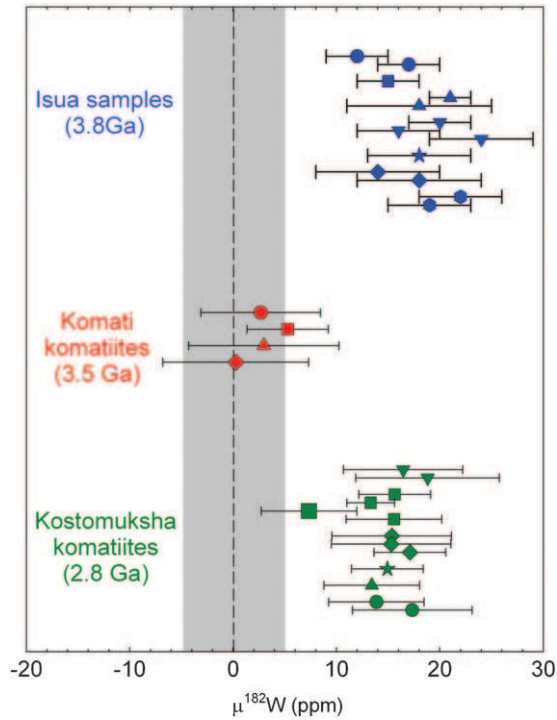

Figure 3.4 High-precision $\mu^{182}W$ measurements of Archean terrestrial samples. The blue symbols correspond to the 3.8 Ga Isua samples (Willbold *et al.*[61]) the red symbols to the 3.5 Ga komatiites from Komati and the green symbols to the 2.8 Ga komatiites from Kostomuksha (Touboul *et al.*[63]). Each symbol represents a different sample and identical symbols indicate replicated analysis of the same sample. Note the 2δ external reproducibility (grey box) of the new analytical techniques ($\sim \pm 5$ ppm), which is about ~ 6 times better than earlier measurements (see Figure 3.3).

the existence of subtle, previously undetectable ^{182}W heterogeneities (Figure 3.4). Willbold *et al.*[61] first reported 13 ± 4 ppm 182W enrichments in rocks 3.8 Ga old from the Isua greenstone belt (Greenland). These positive ^{182}W anomalies were interpreted as reflecting the tungsten isotope composition of the Earth's mantle before the addition of extraterrestrial materials *via* late accretion. This process, which corresponds to the addition of $\sim 0.5\%$ of the total mass of the mantle to Earth by continued accretion of materials with bulk chondritic compositions, subsequent to cessation of core formation, is commonly invoked to account for the relatively high absolute and chondritic relative abundances of highly siderophile elements (HSE) in the modern mantle (*e.g.* Walker[62]). Touboul *et al.*[63] also found 15 ± 4 ppm ^{182}W excesses in 2.8 Ga komatiites from the Kostomuksha supracrustal belt (Baltic Shield) but no ^{182}W anomaly in 3.5 Ga komatiites from Komati (South Africa). Compared to highly metamorphosed rocks from Isua, komatiites are better

preserved and have well-behaved HSE systematics, making it possible to access HSE abundances of their mantle source. The mantle source of Kostomuksha komatiites has 80% of total HSE content relative to the modern mantle, inconsistent with a mantle source that has been preserved from late accretion. Positive ^{182}W anomalies in Kostomuksha komatiites instead reflect the presence, in their mantle source, of a component derived from a reservoir with a high hafnium/tungsten ratio which formed less than 60 Ma after solar system formation. This represents either a deep mantle region that underwent metal-silicate equilibration, or a product of large-scale magmatic differentiation of the mantle. The preservation, in rocks dated at 2.8 Ga, of isotopic anomalies produced during the first 60 million years of solar system history implies that Earth was never totally molten early in its history, even subsequent to the Moon-forming giant impact. During this time convection was much more sluggish than so far considered,[64] allowing isotopic signatures to be preserved, perhaps to the present day.[65]

3.4.3.4 *Meteorite Dating*

The fractionation of hafnium from tungsten is not restricted to planetary differentiation but also occurs among the constitutive minerals of many meteorites and some of their components, making it possible to obtain a precise internal isochron. Owing to its high closure temperatures (*e.g.* between 800 and 900 °C in H chondrites), the hafnium–tungsten system provides time constraints on the earliest high-temperature evolution of planetesimals. Combined with thermal modelling, ages determined using hafnium–tungsten internal isochrons indicate that the H chondrite parent body accreted ~2.5 Ma[66] and the acapulcoite–lodranite parent body ~1.5–2 Ma after solar system formation.[67] Coupled with hafnium–tungsten ages of ~1 Ma for differentiation of the parent bodies of magmatic iron meteorites, these chronological constraints reveal an inverse correlation between accretion age of asteroids and peak temperature in their interiors, suggesting that the different thermal histories of most meteorite parent bodies primarily reflect variations in their initial abundance of heat-producing radioisotopes (*e.g.* ^{26}Al), which is determined by their accretion time. Nevertheless, impact-related processes are an important heat source for the subsequent evolution of asteroids. For instance, the ages obtained from hafnium–tungsten internal isochrons of winonites[68,69] and from tungsten isotopic composition of eucrite metals[70] postdate solar system formation by ~15 Ma and ~20 Ma respectively and probably reflect shock-related secondary perturbation evidenced by the fact that almost all eucrites are breccias.

3.4.4 ^{146}Sm–^{142}Nd Isotope System

3.4.4.1 *Introduction*

The ^{146}Sm–^{142}Nd isotope system consists of two highly refractory elements belonging to the rare earth group. The half-life of ^{146}Sm has been recently

revised and the new value of 68 Ma[71] replaces the older value of 103 Ma. Deviations of the $^{142}Nd/^{144}Nd$ ratio are always very small and the analytical precision was a critical issue in the development of the systematics. Samarium and neodymium have very close partition coefficients and, like most of the short-lived systems, the initial abundance of the parent element was very low. This is why the ^{146}Sm–^{142}Nd systematics have mainly been investigated during the past decade, with the development of the new generation of thermal ionisation mass spectrometers allowing a precision of ± 5 ppm for the $^{142}Nd/^{144}Nd$ ratio.

3.4.4.2 *Early Silicate Differentiation and Mantle-Crust Evolution*

This systematics offers a unique opportunity to investigate early silicate differentiation. The samarium/neodymium ratio generally is not changed during condensation processes and since these elements have no affinity for the metal phase, core formation processes would not modify this ratio either. However, because neodymium is slightly more compatible than samarium during magmatic processes (partial melting and fractional crystallisation), they can be used for tracing silicate differentiation and mantle-crust evolution. Measurement of the ^{142}Nd isotope can then provide powerful indications on the Hadean period ($\sim$the ^{146}Sm lifetime), a geological period still largely unknown because of the scarcity of very old rock records.

^{142}Nd data is now available for a large range of terrestrial samples including rocks collected in the oldest terranes as well as more recent samples collected in a large range of tectonic settings.[72–77] Small deviations of the $^{142}Nd/^{144}Nd$ ratios, lower than 20 ppm relative to the neodymium terrestrial standard, have been measured in samples collected in two areas: the Itsaq complex in south-west Greenland[73,78–82] and the Nuvvuagittuq Greenstone Belt in northern Quebec, Canada (Figure 3.5).[83–85] The age of the differentiation event is calculated by coupling data obtained on both ^{146}Sm–^{142}Nd and ^{147}Sm–^{143}Nd systematics. Because resolving the age equations requires different assumptions (composition of the Earth at the time of silicate differentiation, single differentiation event) the age of the differentiation event cannot be precisely defined but it must have occurred in the first 150 Ma of the solar system's history. Both excesses and deficits in ^{142}Nd have been measured, suggesting that early-formed chemically differentiated reservoirs would have been formed during the crystallisation of a terrestrial magma ocean following the giant impact event forming the Moon. So far no ^{142}Nd anomalies have been detected in samples younger than 3.4 Ga, suggesting that no early-formed samarium/neodymium chemical heterogeneities have been preserved in the convective mantle during more than 1 Ga.

Boyet and Carlson[86] showed that chondrites, which are assumed to be the building blocks of rocky planets, have an average $^{142}Nd/^{144}Nd$ ratio $\sim$20 ppm lower than terrestrial samples. They explain this isotope signature

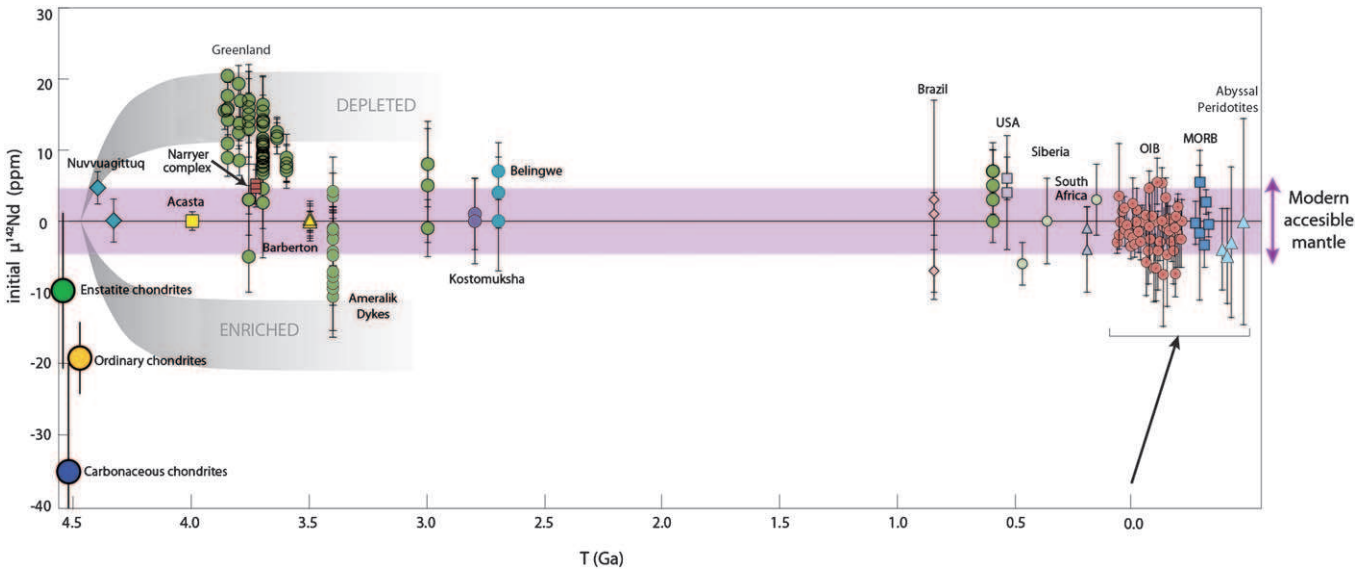

Figure 3.5 Compilation of all published initial $^{142}Nd/^{144}Nd$ ratios for terrestrial samples. Figure modified from Rizo *et al.*;[82] the data sources are cited in the text. Means for chondrites are from Gannoun *et al.*[90] Measured $^{142}Nd/^{144}Nd$ ratios for chondrites are corrected to a common $^{147}Sm/^{144}Nd$ ratio of 0.196. Ages of chondrite formation are not respected in this figure. The grey shaded area in the middle represents the external analytical error of ± 5 ppm. Positive ^{142}Nd anomalies are formed in a mantle source depleted in incompatible elements (high samarium/neodymium ratio) and formed during the ^{146}Sm lifetime. Contrarily, a source enriched in incompatible elements will develop through time deficit in ^{142}Nd.

by a global differentiation of the silicate Earth within 30 Ma of the Earth's formation. The ^{142}Nd signature of terrestrial samples requires that a complementary reservoir has been stored and isolated from the convective mantle since its formation. Alternative scenarios propose that the chondritic model is not appropriate for the bulk silicate Earth.[87] More detailed investigations on chondritic material have revealed that different groups of chondrites have different ^{142}Nd isotope compositions.[88–90] These results confirm that the estimated ^{142}Nd/^{144}Nd ratio of the bulk Earth changes according to the group of meteorites considered. In conclusion, recent studies based on the measurement of stable neodymium and samarium isotope ratios highlight the difficulty of interpreting the ^{142}Nd difference between terrestrial samples and chondrites. The incomplete mixing of material formed in different stellar environments creates significant ^{142}Nd variation and the initial isotope composition of the Earth remains difficult to assess.

3.5 Radioactivity of Long-Lived Chronometers

The development of modern physics would not have been possible without reliable chronometers. In earth sciences, the geological timescale is different from that of humans, requiring appropriate chronometers for us to be able to measure geological history. The development of geochronology was a great breakthrough in being able to quantify geological time. It is now recognised that the Precambrian represents about 90% of Earth's history, although it was limited to a couple of pages in old geological textbooks. The development of geochronology could be the topic of a separate book and so here the discussion is limited to general principles of radiogenic isotopes.

3.5.1 Principles of Isotope Dating

The main principle is as follows: if one can estimate the quantity of radiogenic daughter and radioactive parent isotopes, and knowing the decay constant λ, it is possible to calculate the age of the system since its formation, based on the Curie–Rutherford–Soddy equation introduced above (equation 3.7). This equation may be transformed as following:

$$t = \frac{1}{\lambda} \ln \left\{ \left[\frac{D(t) - D(0)}{P(t)} \right] + 1 \right\} \tag{3.17}$$

The only problem is knowing the D(0) component of the system, *i.e.* the initial quantity of daughter isotope present in the system before the 'radioactive clock' started and produced the purely radiogenic part of the same isotope. To overcome this difficulty, a concrete example of the rubidium–strontium isotope system is presented in the following section.

It is important to note, however, that the system should have remained closed since its formation, with nothing going in or out. This can be applied to any geological object, *i.e.* rocks, minerals, the Earth, the solar system, *etc.*

3.5.1.1 Rubidium–Strontium System

Rubidium has two natural isotopes: ^{85}Rb and ^{87}Rb (27.8%). The latter is radioactive and produces the ^{87}Sr radiogenic isotope by beta-minus decay: $^{87}Rb \rightarrow {}^{87}Sr + \beta^-$.

Strontium consists of four stable isotopes in the following proportions: ^{84}Sr(0.56%), ^{87}Sr(7.0%), ^{86}Sr(9.9%), and ^{88}Sr(82.6%). Only ^{87}Sr is radiogenic, produced by radioactive decay of rubidium. According to equation 3.7 the present-day ^{87}Sr concentrations obtained are:

$$^{87}Sr = {}^{87}Sr_0 + {}^{87}Rb(e^{\lambda t} - 1) \quad (3.18)$$

Given that the mass spectrometer allows measurement of the isotopic ratios (see section 3.2), it would be convenient to transform equation 3.8 by dividing each member by the non-radiogenic strontium isotope ^{86}Sr, assuming that $^{86}Sr_0 = {}^{86}Sr_t$ (where 0 = initial time and t = present time). Doing this, one obtains:

$$\left(\frac{^{87}Sr}{^{86}Sr}\right)_t = \left(\frac{^{87}Sr}{^{86}Sr}\right)_0 + \left(\frac{^{87}Rb}{^{86}Sr}\right)_t \left(e^{\lambda t} - 1\right) \quad (3.19)$$

Note that this equation contains an elemental ratio (*i.e.* rubidium–strontium) which often limits the precision; this is not the case for the Pb–Pb system. For a fixed value of t, (3.19) is an equation of a straight line (with variables $^{87}Sr/^{86}Sr$ and $^{87}Rb/^{86}Sr$) which can be transformed as:

$$Y = Y_0 + X(e^{\lambda t} - 1) \quad (3.20)$$

The decay constant λ for rubidium is known (Table 3.3), thus the $(e^{\lambda t} - 1)$ term, which represents the slope of the isochron, is a constant value because it is similar for all samples of the same age. The initial ratio at the time of system formation, $(^{87}Sr/^{86}Sr)_0$, may be estimated from this equation.

To obtain the straight line, at least two samples with different $^{87}Rb/^{86}Sr$ ratios should be analysed. Taking into account the analytical uncertainty, more than two samples should be analysed to obtain better precision, verify the accuracy of the results, and check if the system has stayed closed during the decay. It could be either different minerals from the same rock with different $^{87}Rb/^{86}Sr$ ratios or samples of different lithology from the same geological formation in order to obtain quite a large spectrum of $^{87}Rb/^{86}Sr$ ratios. The rubidium–strontium system has been one of the major chronometers used to date the returned Moon samples.[91] In recent years, however, the use of the rubidium–strontium dating technique has been restricted

mostly to the study of planetary material and it is now seldom used for terrestrial systems because of its sensitivity to open behaviour during alteration processes.

3.5.2 Uranium–Lead Isotope System

3.5.2.1 Decay Constants

One reason the uranium-lead method is so powerful is that unlike other radioisotopic systems, multiple isotopes of the same element are measured and act on a cross-check on each other, and have decay schemes that are well-constrained. ^{238}U decays to stable daughter ^{206}Pb with a half-life of $4.4683 \pm 0.0024 \times 10^9$ years; ^{235}U decays to stable daughter ^{207}Pb with a half-life of $7.0381 \pm 0.0046 \times 10^8$ years, measured by direct decay counting by Schoene *et al.*[92] The decay constant ($\ln_2/t_{1/2}$) of ^{235}U has been refined empirically by Mattinson[93] to $0.98671 \pm 0.00012 \times 10^9$ years^{-1}, within the uncertainties of Schoene *et al.*[92] but improving their $\sim$0.1% precision. Though imperfect (see *e.g.* Schoene *et al.*[94]), these fundamental parameters for the calculation of ages based on isotopic ratios are better established than other radioisotopic systems. ^{208}Pb results from the decay of ^{232}Th, and ^{204}Pb is not radiogenic, and so has a roughly constant abundance on Earth (except for extraterrestrial sources), presently about 1.4%.

3.5.2.2 Analytical Techniques

Different analytical techniques are used in uranium–lead geochronology. The most accurate and precise of these is isotope dilution thermal ionisation mass spectrometry (ID-TIMS). First applied to zircon ($ZrSiO_4$) geochronology in the 1950s,[95–97] ID-TIMS refers to the measurement on a thermal ionisation mass spectrometer of a sample that has been spiked with an isotopic tracer. This method is insensitive to mass spectrometric sensitivities and abundance, and because of the tracer it is not reliant for calibration on external standards, which must themselves be well characterised isotopically. Precision is therefore limited primarily by the instrument, and can be better than 0.1%. When applied to zircon, and using appropriate laboratory techniques, ID-TIMS uranium–lead dating of zircon can reliably produce ages virtually throughout geological time at $\sim \pm 1$ Ma or better, making it uniquely powerful among radioisotopic geochronological methods. Compston *et al.*[98] applied secondary ionisation mass spectrometry (SIMS) to geochronology with the development of the sensitive high-mass resolution ion microprobe (SHRIMP), which uses a beam of oxygen ions to ablate a small pit $\sim$20 μm in diameter and a few microns deep, the contents of which are then analysed by a sector mass spectrometer. Precision is limited to about 1%, due to the small sample being measured and the reliance upon external calibration standards. Laser-ablation inductively coupled mass spectrometry (LA-ICPMS) has been more recently employed as an *in situ* method for

uranium–lead geochronology. This has similar limitations to the SHRIMP though poorer sensitivity hampers precision; however, it is a fast and relatively inexpensive method that is has seen an increase in use recently. The *in situ* methods are most useful when there is a need for rapid analysis of many grains (*e.g.* detrital mineral analysis), when the crystal must be preserved for other geochemical analyses, or when cost is a factor. TIMS produces more precise ages, but completely destroys the sample, requires clean laboratory work and laborious chemical procedures, and is therefore more expensive.

An important advance has been the realisation, illustrated by Mundil *et al.*,[99] that ages obtained from multi-crystal zircon fractions (where several mineral grains are dissolved together and analysed in bulk) may not be accurate. Multi-crystal fractions have been used in order to improve the strength of the radiogenic lead signal and therefore improve analytical precision. However, it is apparent that analysing a population of grains that may include both older, xenocrystic or inherited grains and apparently younger grains that have suffered varying degrees of lead loss will yield an average that may be concordant, but inaccurate. Therefore, single-crystal analyses have become the standard in obtaining ages that may be assessed realistically and with statistical rigour, though even single grains can include inherited cores, or may themselves produce an age that represents an average of a protracted growth history, *e.g.* in a magma chamber (residence time).

3.5.2.3 *Dating Applications of the Uranium–Lead Technique*

In recent decades, advances in technology and in our understanding of mineralogical and petrological processes have led to the uranium–lead system becoming the benchmark in geochronology, at present the method capable of obtaining the most precise and accurate age information on most minerals. Common accessory phases that are used include titanate, monazite, apatite, xenotime, perovskite, and others, though these minerals contain initial lead which must be corrected for.

Minerals such as zircon ($ZrSiO_4$) and baddeleyite (ZrO_2) incorporate uranium and, to a lesser extent, thorium into their crystal structure during growth (typically 10–1000 ppm uranium), and exclude most other elements, including lead. This means that virtually all lead in these minerals is radiogenic, and corrections for initial lead are negligible. For this reason these minerals, of which zircon is more common, are preferred for use in uranium–lead geochronological analysis.

Closure temperatures for the uranium–lead isotopic system are typically high ($\sim$900 °C for zircon,[100] and at least that for baddeleyite; see *e.g.* Davidson and Breemen[101]) and it is important to bear this in mind when comparing age results with those obtained from other isotopic systems. The uranium–lead age is generally the high-temperature constraint on the formation of a geological unit, and can also reflect hydrothermal events,

detrital or inherited histories, or various stages in the development of magma bodies, as reflected in the growth of mineral phases.

Generally speaking, the uranium–lead dating method can be applied to any mineral that contains uranium. For example, CAIs in meteorites have been used to date the oldest solids formed in our solar system,[102] and authigenic xenotime has been used to date sedimentary rock formation.[103] Hydrothermal events, such as those related to ore-forming processes, have been dated using hydrothermal zircon or rutile.[104] Ore deposits have been dated using columbite,[105] or monazite[106] grown *in situ* during the formation of these deposits. Uranium–lead dating has been applied to Quaternary materials,[107,108] and to the oldest continental Earth materials known, detrital zircons from the Jack Hills of Western Australia.[109]

The high precision possible with this method enables the resolution of magmatic events that were not previously distinguishable from one another, and when used in parallel with lower-temperature geochronometers such as the ^{40}Ar–^{39}Ar method allow the creation of thermal histories of magmatic systems.[110] It allows the establishment of connections between magmatic events and biotic crises such as mass extinctions,[111] and of a geological timescale based upon absolute ages determined with high precision.[112]

As long as uranium-bearing minerals can be extracted from a rock, whether it is baddeleyite from a basalt, zircon from a granite, or perovskite from the mantle, the uranium–lead method can be used to obtain a reliable age for the material. Care must be taken in interpreting the data in order to ensure that a system closed to lead and uranium is maintained, or at least that open-system behaviour is understood.

3.5.3 Potassium–Argon and $^{40}Ar/^{39}Ar$ Dating Techniques

3.5.3.1 Potassium–Argon Technique

The potassium–argon technique is based on the natural radioactive decay of ^{40}K to $^{40}Ar^*$ and $^{40}Ca^*$ with a combined half-life of $\sim$1.25 Ga. Because potassium is in solid form and argon is a gas, potassium and argon must be measured using different machines on different aliquots. Potassium is mostly measured using either flame photometry or isotopic dilution and argon is measured using a noble gas spectrometer. This method, however, encounters immediate limitations as (1) it requires relatively large aliquots to homogenise the sample composition, (2) there is no way of determining if the sample has remained closes to external perturbations (*e.g.* alteration, recrystallisation) or (3) has incorporated initial ^{40}Ar and ^{36}Ar with a composition different from the assumed $^{40}Ar/^{36}Ar$ atmospheric ratio ($\sim$299).[113] This technique has been progressively replaced by the ^{40}Ar–^{39}Ar approach over the years, except in a few cases such as the dating of clay where the ^{40}Ar–^{39}Ar technique has technical limitations and the potassium–argon technique is still better suited.

3.5.3.2 ^{40}Ar–^{39}Ar Technique

The methodology behind the ^{40}Ar–^{39}Ar technique represents a drastic improvement over the potassium–argon method. In essence, the idea is to transform ^{39}K into ^{39}Ar by bombarding the sample with neutrons in the core of a nuclear reactor. As a result, the measurement of the $^{40}Ar/^{39}Ar$ ratio makes it possible to calculate an age by comparison with a standard of a known age. For the interested reader, the technique is described in greater detail in the book by McDougall and Harrison.[114] The direct advantage of this approach is the ability to measure an age using a single grain of a given sample, thus circumventing sample heterogeneity. More importantly, step-heating *via* laser or furnace allows obtaining a detailed distribution of the $^{40}Ar/^{39}Ar$ ratio in the sample and testing if the sample has been perturbed after its formation, or if a robust age can be extracted from the set of analyses. When the $^{40}Ar/^{39}Ar$ ratio is homogenous throughout most of the age spectrum, it yields a so-called plateau. A plateau age is a succession of steps including at least 70% of the total ^{39}Ar gas released and giving the same $^{40}Ar/^{39}Ar$ ratio, and hence the same age. Such a plateau can only be achieved through stringent sample preparation where samples must be devoid of alteration products and must be homogenous. Otherwise, structured profiles usually indicate processes such as thermally activated diffusion loss of $^{40}Ar^{*}$, alteration, excess $^{40}Ar^{*}$, mixture of phases with different time–temperature histories, and ^{39}Ar or ^{37}Ar recoil processes.[114] The step-heating approach, combined with stringent statistical ξ^2-tests (MSWD and *P*-values where $P \geq 0.05$) to define a plateau (*e.g.* Baksi[115]) represents a robust and objective mean of testing the validity of an age. The problem of inherited or excess argon (*i.e.* parentless ^{40}Ar present in the system at the time of formation) can be in most case easily addressed using the inverse isochron approach, which, contrary to the plateau age spectrum approach, does not assume the composition of the trapped $^{40}Ar^{*}$ but measured it directly *via* the $^{40}Ar/^{36}Ar$ ratio. Hence, for rocks containing abundant amount of trapped ^{40}Ar, the inverse isochron approach is usually preferred. Note that the same statistical tests employed for the plateau method are applicable to the inverse isochron approach.

3.5.3.3 Decay Constants

Until recently, ^{40}Ar–^{39}Ar (and potassium–argon) ages were calculated using the decay constants ($^{40}Ar^{*}$ and $^{40}Ca^{*}$) recommended by Steiger and Jäger.[116] Over the years, argon geochronologists noted that the ^{40}Ar–^{39}Ar ages seem to be systematically younger by about 1% compared to the ^{238}U–^{206}Pb ages (*e.g.*[117,118]). As such, a recent study by Renne *et al.*[119] using ^{40}Ar–^{39}Ar and ^{238}U–^{206}Pb data from rocks that have recorded the same event, and direct activity measurement of the ^{40}K total decay constant, led to the calculation of a new set of ^{40}K decay constants. Due to the joint use of both the ^{238}U decay constant and the measured ^{40}K activity, the set of decay constants proposed

by Renne *et al.*[119] make it possible to calculate ^{40}Ar–^{39}Ar ages that, for potassium-rich minerals, are equally (or in some cases more) precise than uranium–lead ages measured with TIMS, at least for the Phanerozoic period. For example, Renne *et al.*[119] showed that the age of the Permo–Triassic boundary measured using sanidine ^{40}Ar–^{39}Ar step-heating analyses is 252.3 ± 0.4 Ma by comparison with zircon ^{238}U–^{206}Pb ages of 253.4 ± 0.4 Ma (both ages include all source of errors and are reported at 2σ).

3.5.3.4 Dating Applications of the ^{40}Ar–^{39}Ar Technique

In essence, ^{40}Ar–^{39}Ar dating can be applied to all minerals and rocks that contain a measurable amount of potassium oxide (*e.g.* sanidine, micas), from few thousand years old (*e.g.* Renne[120]) to as old as the solar system itself (4.56 Ga; cf. review by Bogard[121]), but in theory there is no real older limit. Even minerals with very low abundance of potassium oxide, such as plagioclase or pyroxene, can be analysed and yield accurate age data, albeit generally less precise than for potassium-rich minerals. Broadly speaking, potassium oxide concentration generally correlates with analytical precision. Because most crustal minerals contain potassium oxide, ^{40}Ar–^{39}Ar dating is applicable to a large range of geological processes. A good example of the range of possible applications is given by various papers in the book by Jourdan *et al.*[122] In the following sections we provide a few examples of the most common applications.

Planetary Sciences. ^{40}Ar–^{39}Ar dating can be applied to the study of planets, moons, and asteroids. In particular, it is relevant to the study of the bombardment, volcanic, and time–temperature histories of any planetary body.[121,123,124] Due to its sensitivity to moderate thermal perturbations, the ^{40}Ar–^{39}Ar technique is particularly well suited to the dating of major hypervelocity impact events. For example a well-defined age of 4507 ± 20 Ma has been recorded in plagioclase from a eucrite meteorite thought to come from the asteroid 4 Vesta.[125] High-precision dating of lunar (impact) melt breccia has shown that most ^{40}Ar–^{39}Ar ages cluster around 3.8–4.0 Ga,[126] possibly suggesting an increase in the bombardment of the Moon at that time.[127] Impacts have also been recorded in spherules formed during rapid quenching of silicate melt during impact. ^{40}Ar–^{39}Ar analyses of hundreds of spherules recovered from three distinct Apollo landing sites have yielded ages ranging from 4.4 Ga to the present, indicating the constant bombardment of the Moon since its formation.[128–130] Furthermore, these studies have shown an abundance of spherules with ages older than 3–2.5 Ga and a sharp spike of spherules with ages younger than about 400 Ma.

If the system has not been perturbed by impact events, then the ^{40}Ar–^{39}Ar technique can be applied to date extraterrestrial basaltic eruptions (see *e.g.* Cohen *et al.*[131]) and the cooling rate of asteroids.[132] For example, Jourdan[124] reinterpreted the ^{40}Ar–^{39}Ar data obtained on lunar basalts from the Mare

Crisium by Cohen *et al.*[131] to illustrate a sequence of four eruptions with well-defined ages between about 3.22 and 3.33 Ga.

Volcanic Eruptions. The entire range of volcanic products can be dated with the ^{40}Ar–^{39}Ar technique, from basalts to rhyolitic tuffs. Young rocks between a few thousand years old and up to a few tens of millions of years can be dated on groundmass with excellent accuracy and good precision,[133,134] and the technique has been applied to problems such as the study of an active volcanic island like Hawaii.[135] For rocks older than ~30 Ma, it is preferable to isolate datable minerals due to the increasingly undesirable effect of pervasive alteration, and where alteration products are hard if not impossible to remove from groundmass.[136,137] For basalts older than 30 Ma, the target mineral by default is plagioclase. Because plagioclase contains only around 0.05% of potassium oxide, it generally provides ages that are not the of utmost precision. On the other hand, plagioclase data can be very accurate, as the presence of sericite alteration can be easily identified on these phases using a step-heating approach.[137] Plagioclase ^{40}Ar–^{39}Ar dating is widely used in the investigation of the duration timing of large igneous provinces (*e.g.* [138–141]). ^{40}Ar–^{39}Ar dating of basalts has largely contributed to the idea that large igneous provinces have been responsible for mass extinctions throughout Earth's history, due to their identical timing.[142]

For more evolved rocks, minerals such as hornblende, biotite, or sanidine yield very precise and robust ages (Figure 3.6). For example, the dating

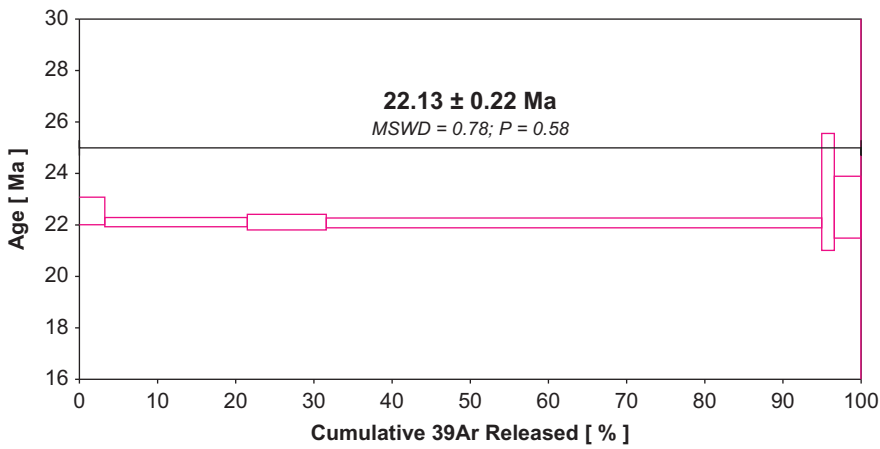

Figure 3.6 Example of ^{40}Ar–^{39}Ar age spectra where the individual steps are plotted as a function of the ^{39}Ar released. The ^{40}Ar–^{39}Ar plateau age has been obtained on sanidine from a syenite volcanic rock (Africa). Unpublished data from the archive of F. Jourdan. Note, the uncertainty is reported at 2δ and includes all sources of errors. The mean square weighted deviation (MSWD) and P values indicated that this age is statistically valid.

of sanidine has been recently used to obtain an age of 73.9 ± 0.6 ka (2σ) for the infamous Toba supereruption.[143] Such precision can be very important when studying processes such as the risks associated with a given volcanic region. ^{40}Ar–^{39}Ar dating of volcanic products, in particular pyroclastic tuffs rich in sanidine, is important to calibrate the geological timescale and crucial in pinpointing the age of archaeological artefacts by dating bracketing volcanic layers (*e.g.* the age of the *Australopithecus* Lucy at 3.18 ± 0.01 Ma.[144]

Thermochronology Applied to Tectonic Processes. One of the major applications of the ^{40}Ar–^{39}Ar technique relies on the various closure temperatures of different minerals. The closure temperature is an approximate temperature below which a given mineral will start to retain most of its radiogenic $^{40}Ar^*$. ^{40}Ar–^{39}Ar thermochronology studies can be applied to a range of ubiquist minerals with distinct closure temperatures ranging from up to ~ 600 °C (hornblende) down to ~ 150 °C (feldspar).[114] Each mineral will give the age at which it reached its closure temperature. In other words, the higher the closure temperature, the older the apparent age, except in the case where all the apparent ages are indistinguishable, indicating extremely fast cooling. This behaviour is usually observed when a rock cools down to ambient temperature after having undergone deformation or slow cooling. This property is abundantly exploited during the study of orogeny (mountain formation), when rocks are usually strongly deformed through metamorphism process and follow complex time–temperature histories. Such histories can be recovered by analysing a suite of minerals with different closure temperatures, and/or by inverting results from age spectra that display clear diffusion profiles (*i.e.* progressive $^{40}Ar^*$ loss). Major orogens have been studied with this approach such as the relatively recent Himalaya and Alps chains,[145–147] or much older orogens such as the Paleoproterozoic Mt Wood Inlier in Australia[148] or the East African Orogen in Mozambique.[149]

Mineral Deposits. ^{40}Ar–^{39}Ar is a powerful tool for dating mineral deposits. In essence, several key potassium-rich minerals tend to form during the hydrothermal process associated with many ore deposits (*e.g.* copper, gold, molybdenum). For example, intrusive-related mineral and metal deposits are associated with porphyry bodies and epithermal processes. Hydrothermal alteration, consisting of one or several temporally distinct pulses, can be dated using the ^{40}Ar–^{39}Ar technique using minerals such as sericite (alteration of plagioclase),[137] adularia,[150,151] and alunite, all of which have been successfully used in several ^{40}Ar–^{39}Ar studies related to the timing of ore deposits. For example, gold mineralisation in the Liba goldfield (China) has been dated at 216.4 ± 0.7 Ma using hydrothermal mica minerals.[152] Although the minerals mentioned above tend to yield well-defined plateau ages, the real difficulty resides in the interpretation of those ages. Indeed, one needs to keep in mind that what is really

dated is the formation of these minerals during hydrothermal activity. If the hydrothermal activity is brief, on the order of a few hundred thousand years, then the age of the confidently dated mineral gives the age of the ore formation. On the other hand, if the hydrothermal activity is episodic and lasts over a few million years, then the ^{40}Ar–^{39}Ar age can provide a range of possible ages within this timeframe. This range includes the age of the end of the hydrothermal activity, which can be a few million years younger than the age of the ore formation itself. Such a phenomenon has been observed, for example, for the Xihuashan tungsten deposit in China.[153]

3.5.4 Lutetium–Hafnium Isotope System

3.5.4.1 Introduction

The behaviour of the whole-rock samarium–neodymium isotopic system in magmatic rocks closely parallels that of the whole-rock lutetium–hafnium system,[154,155] and the latter is strongly controlled by the mineral zircon. Once it crystallises from a magma, zircon is stable up to high metamorphic grades, and because of its very low lutetium/hafnium ratio, can preserve the $^{176}Hf/^{177}Hf$ ratio of the host magma at the time of crystallisation. Thus the link between the age and the isotopic composition of the magma is more likely to be preserved than in whole-rock isotopic systems. High values of $^{176}Hf/^{177}Hf$ indicate a 'juvenile' or mantle-derived origin for the magma, while low values imply the reworking of older crustal material. Recent studies of oxygen and hafnium isotopes in single zircon grains[156] have shown that a high $^{176}Hf/^{177}Hf$ ratio is linked with mantle-like oxygen-isotope values. These studies confirm the utility of hafnium isotope data in distinguishing between juvenile and recycled components in crustal rocks. However, more detailed work is needed to understand the oxygen–hafnium systematics of crustal recycling processes, and to use these data to better constrain the range of hafnium isotope compositions that represents juvenile sources.

3.5.4.2 Interrelation with Other Isotopic Systems

Zircon is a common accessory mineral in many igneous rocks, and has become one of the most important tools in the earth sciences; thousands of grains are analysed yearly in laboratories worldwide, mainly for dating. The isotopic systematics of oxygen and the uranium–thorium–lead and lutetium–hafnium systems in zircon provide a range of information on the age and sources of melts and have been extensively used for studying processes of crustal and mantle evolution.[157–159] *In situ* microanalysis of the uranium–lead system allows us to measure the age of an individual zircon grain. The isotopic composition of hafnium and oxygen can tell us whether a magmatic rock was generated in the mantle, or by remelting of older crust.

3.5.4.3 Application for Crustal–Mantle Evolution

The lutetium–hafnium system in zircon therefore is a powerful tool for studying processes of crustal and mantle evolution,[155,160–165] and new technology makes if feasible to do this on a global scale. To understand the growth of a crustal block, we need to determine the sources of magmatic material over its history: whether it was juvenile (derived from the convecting mantle or from recently formed crust) or recycled (remelting of older crust), or possible a mix of those two. Early models of crustal evolution made extensive use of the samarium–neodymium isotopic system; age data (typically from uranium–lead dating of zircons) were combined with neodymium isotope analysis of the host rocks to define the source material. This approach is powerful, but it has several drawbacks: it is time consuming, so data for any area are necessarily concentrated on relatively few selected samples, and the whole-rock samarium–neodymium system is prone to disturbance by metamorphism or weathering.

A number of recent studies have provided extensive datasets on a global scale; one of these, by Belousova,[166] used 23 000 analyses. This study took a new approach to the modelling of hafnium isotope data, and came to two major conclusions, each of which broke with conventional thinking:

- At least 70% of all exposed continental crust was originally generated in Archean time (>2.5 Ga; Figures 3.7 and 3.8) and has been reworked to different degrees during younger tectonic events.
- The prominent peaks in the age distribution of zircon-bearing rocks do not reflect periods of net crustal growth, but simply record magmatic activity that largely reworked pre-existing crust.

This study treated the zircon database on a worldwide scale. It was followed by one[167] that used the paleogeographic distribution of different hafnium isotope signatures in specific time intervals, to identify and analyse two fundamentally different tectonic systems that have organised Earth's crustal evolution for at least the last 500 million years.

3.5.5 ^{190}Pt–^{186}Os and ^{187}Re–^{187}Os Isotope Systems

3.5.5.1 Introduction

In the past decade, as a result of tremendous analytical advances, the rhenium–osmium and platinum–osmium isotopic systems have seen an explosion of applications in geochemistry and cosmochemistry. ^{187}Re decays to ^{187}Os with a half-life of 41.6 Ga, whereas ^{190}Pt decays to ^{186}Os with a half-life of 469 Ga (Table 3.3). Both systems are unique in that rhenium, platinum, and osmium belong to the HSE, *i.e.* they strongly partition into metal or sulfide liquid relative to silicate melt. As a result, these elements were nearly quantitatively extracted from silicate parts of planetary bodies into

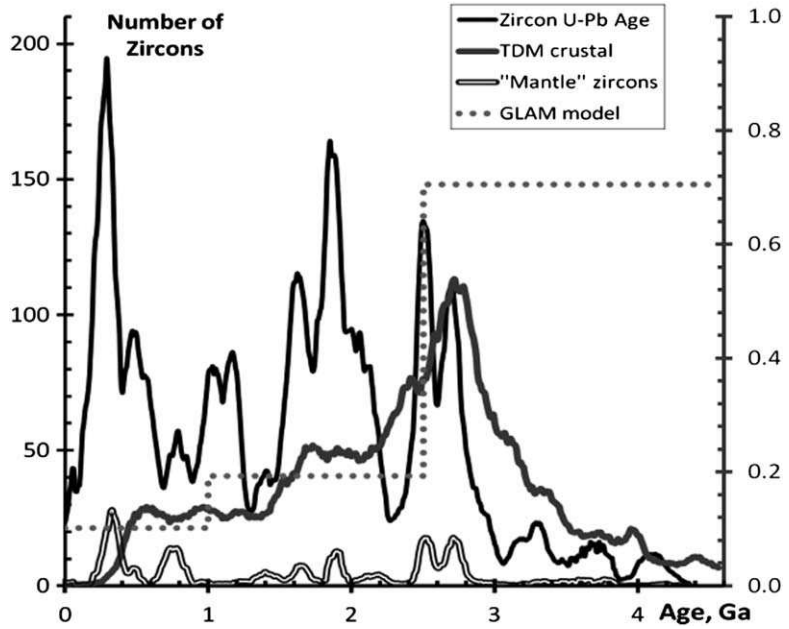

Figure 3.7 Relative probability curves (left scale) of uranium-lead zircon ages), T_{DM}^{C} model ages and number of zircons with juvenile hafnium isotope compositions (defined as grains with $\varepsilon_{Hf} > 0.75 \times \varepsilon_{Hf}^{DM}$). Proportions of the continental lithosphere formed during three major time intervals derived from GLAM mapping (Belousova *et al.*[166]) are shown by the dashed line (right axis). A compilation of zircon uranium-lead and hafnium isotope data illustrates the important difference between 'age peaks' and episodes of 'crustal generation'.

cores during planetary differentiation. Additionally, during mantle melting, osmium is compatible with the melting residue, whereas platinum is weakly incompatible and rhenium moderately incompatible during low to moderate degrees of partial melting, such as those involved in generation of basalts. These elements, therefore, can provide unique insights into certain processes, to which the more traditional, lithophile element-based isotopic systems, are not sensitive. These processes include planetary accretion and differentiation, crust–mantle and core differentiation, and core–mantle exchange. Excellent reviews of both isotope systems are available.[168–172] Below, we provide a brief overview of the most common applications.

3.5.5.2 Rhenium–Osmium and Platinum-Osmium Chronometry

The uniqueness of the ^{190}Pt–^{186}Os and ^{187}Re–^{187}Os isotope systems as chronometers stems from their applications to materials that cannot be dated using other isotopic systems. For example, they are the only systems able to date directly metal phases, as has been largely illustrated by the

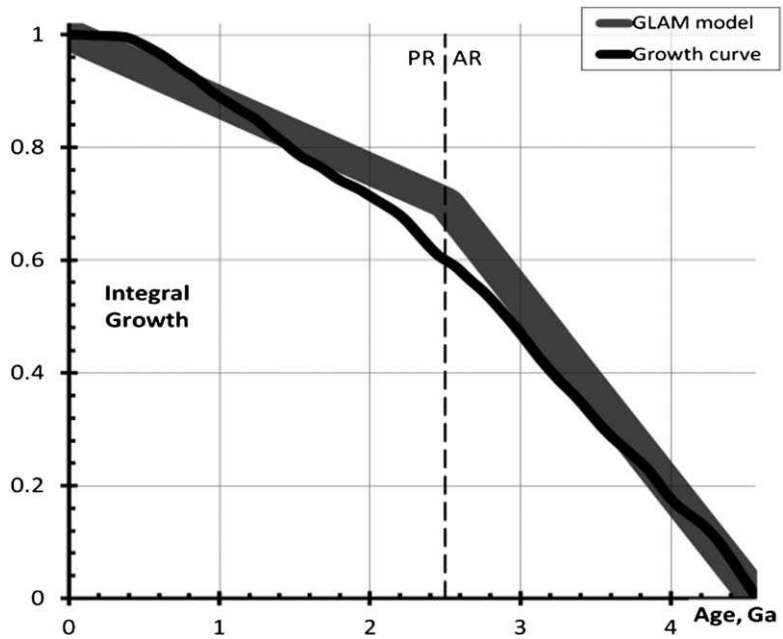

Figure 3.8 The integrated crustal growth curve (black line) using combined uranium–lead and hafnium isotope data, compared with the GLAM model (Belousova *et al.*[166]).

dating of iron meteorites, which, in turn, was the first application of this chronometer. A number of common applications include the following.

Dating Volcanic Sequences Consisting of Mafic-Ultramafic Lavas, Such as Komatiites and Picrites. During differentiation of komatiite and picrite lava flows, osmium is usually compatible with the fractionating mineral assemblage, while both platinum and rhenium are incompatible. This contrasting behaviour results in large variations in platinum/osmium and rhenium/osmium ratios between different portions of individual lava flows, which, in turn, permits generation of isochrons. The latter can be used to obtain precise chronological information, assess closed-system behaviour of HSEs during post-magmatic processes, and precisely determine the initial osmium isotopic compositions and time-integrated rhenium/osmium and platinum/osmium ratios in the sources of the lavas. The correlations between magnesium oxide and HSE, combined with the osmium isotopic data, can also be used to precisely calculate the absolute HSE contents of the sources of komatiite lavas.[173–175]

Dating Ore Genesis. The rhenium–osmium and platinum-osmium isotopic systems can be directly used to study ore-forming minerals, rather than host silicates. One of the first applications of the rhenium–osmium

isotopic system was to date molybdenites, which have very high rhenium and very low osmium concentrations, so that nearly all osmium in the sample is radiogenic. Recent developments in this technique allow accurate and precise chronological information to be obtained.[176] Another important ore mineral is chromite, which, unlike molybdenite, has a very low rhenium/osmium ratio. As a result, this mineral, which is highly resistant to alteration, freezes the initial osmium isotopic composition of the magma it crystallises from, thus providing both chronological and petrogenetic information.[177–179] Finally, sulfides are also widely used to obtain both chronological and petrogenetic information.[172,180–182]

Dating Diamonds. Diamonds often contain sulfide inclusions with high (up to ppm level) osmium concentrations. This allows the rhenium–osmium system to be applied to obtain both chronological and petrogenetic information on single crystals. A recent study of sulfide inclusions in diamonds from the Panda kimberlite in Canada[183] made it possible to trace the source of the diamonds to the fluids rising from the subducting slab and argues for the onset of plate tectonics as early as 3.52 Ga.

Dating Organic-Rich Sediments. One of the peculiar features of the HSE is their affinity for organic-rich matter within sedimentary sequences, such as black shales, coal, and oil-hosting sands. Provided the rhenium–osmium system in such organic-rich materials has remained closed since the time of deposition, a rhenium–osmium study may provide valuable chronological information, as well as help obtain the osmium isotopic composition of the source of organic-rich matter.[184,185]

Dating Oil. The ^{187}Re–^{187}Os isotope system has been successfully applied to petroleum systems in recent years, both as a process tracer using $^{187}Os/^{188}Os$ and as a geochronometer using rhenium–osmium decay relationships. The first detailed report of rhenium and osmium elemental and isotopic systematics in natural crude oils showed that a very high proportion of both elements resides in the asphaltene fraction, and that the $^{187}Os/^{188}Os$ ratio of modern crude oils is highly variable, and broadly correlates with source rock age.[186] These observations allow for application of osmium isotopes as a tracer of source rock identity[187] and of evaluation of fluid interaction following reservoir charging.[188] Importantly, the concentration of osmium in the asphaltene fraction makes the osmium isotope system an ideal tracer for heavy biodegraded petroleum from which traditional tracing information, such as biomarkers, may have been lost. Further experimental work by Rooney *et al.*[189] studied the rhenium–osmium elemental and isotopic relationships between source rock and oil by hydrous pyrolysis. Several studies have shown that ^{187}Re–^{187}Os isotope system is applicable to petroleum systems as a geochronometer. Selby *et al.*[190] first showed that bitumen from the Polaris carbonate-hosted lead–zinc deposit recorded a rhenium–osmium age of $\sim$374 Ma. Bitumen here

is the biodegraded product of migrated oil, interpreted to have charged the carbonate reservoir together with aqueous fluids that produced lead–zinc mineralisation dated at ~366 Ma by the rubidium–strontium method. Mineralisation at Polaris also yields a ~367 Ma palaeomagnetic age, such that three methods independently yield a Late Devonian age fluid flow at Polaris. Subsequently, Selby and Creaser[191] determined a rhenium–osmium age of ~110 Ma for the giant Western Canadian Oil Sands. Finlay *et al.*[187] applied rhenium–osmium geochronology to oils of the UK Atlantic Margin, and determined an age of ~68 Ma for oil generation. This rhenium–osmium age compares well with other independent methods of oil generation dating such as ^{40}Ar–^{39}Ar and basin thermal modelling. Although application of the rhenium–osmium isotope system to petroleum systems is still in its infancy, the potential is large for both process tracer and geochronology.

3.5.5.3 Rhenium–Osmium and Platinum-Osmium Isotope Systems as Tracers of Planetary Processes

Chronometry of Mantle Differentiation Processes. Unlike traditional isotopic systems involving lithophile trace elements, which concentrate in the melt to nearly the same degree and are present in low abundances in mantle residues, osmium is concentrated in mantle residues, whereas rhenium (and platinum) are preferentially incorporated in the melt. This feature of the rhenium–osmium isotopic system has proved uniquely suited to study the history of melt extraction from the mantle.[192] These studies provide evidence for strong correlation between the age of continental crust and the timing of melt depletion and formation of subcontinental, residual mantle. In addition, melts formed during remelting of the latter are important sources of HSE mineralisation.

Crust–Mantle and Core–Mantle Interaction. Oceanic crust, consisting mainly of basalt and sediment, has high rhenium/osmium ratio. Upon returning back into the mantle at the subduction zones, it transforms into eclogite and forms isolated domains that can be stored deep in the mantle for up to 1.8 Ga.[193] Given enough time, these domains will develop highly radiogenic $^{187}Os/^{188}Os$. The presence of aged oceanic crust in the sources of plume magmas, such as ocean island basalts (OIB) and komatiites, can be detected using the rhenium–osmium isotopic system in combination with lithophile trace element and isotopic studies.[194–196] Due to a lower incompatibility of platinum during mantle melting and a much greater half-life of ^{190}Pt, the deviation of $^{186}Os/^{188}Os$ in the aged oceanic crust from the mantle reference will be much smaller compared to $^{187}Os/^{188}Os$. However, some plume-derived lavas show coupled radiogenic initial $^{186}Os/^{188}Os$ and $^{187}Os/^{188}Os$ ratios.[197] In order to explain this correlation, several hypotheses have been put forward, such as core–mantle

interaction[198] or long-term preservation of early mantle differentiation products.[63] Establishing the nature of osmium isotopic anomalies in the mantle is crucial for our understanding of the Earth's geodynamics, its thermal history, and the timing of planetary differentiation.

HSE in Extraterrestrial Materials: Timing of Accretion in the Solar System. Core formation must have nearly quantitatively removed HSE from the silicate portions into cores of planetary bodies, leaving highly-fractionated HSE patterns. However, HSE abundances in the terrestrial mantle are two to three orders of magnitude higher than could be expected from low-pressure metal-silicate partitioning experiments,[199] and the osmium isotopic composition is roughly chondritic,[200] implying long-term chondritic platinum/osmium and rhenium/osmium ratios in the terrestrial mantle. In order to explain this controversy, a late accretion hypothesis was put forward, whereby 0.5–1% of chondritic materials were added to the mantle after the last major equilibration between the core and mantle.[201]

Unlike the dynamic Earth, the surface of the Moon still holds evidence of late accretion in the form of impact craters and impact melt breccias. Studies of osmium isotopic composition and absolute and relative HSE abundances in the impact melts allows reconstruction of the HSE composition of the impactors,[202–204] which has far-reaching implications for understanding the early history of the solar system and the origin of life.

3.6 Environmental Isotopic Tracers

The ability to trace the sources of dust and pollution deposited in a particular region allows an understanding of the atmospheric transport paths that are involved. Often the elemental concentrations and mineralogy of deposited aerosols have been used for this purpose. However, these systems can be altered by environmental processes, *e.g.* changes in accumulation in a region will impact on measured elemental concentrations. Therefore the use of isotopic systematics to characterise dust and pollution has emerged as an important method. Grousset and Biscaye[205] reviewed the use of strontium, neodymium, and lead isotopic systematics to trace sources of natural aerosols and anthropogenic pollution. Lead isotopes have been shown to be particularly successful in the tracing of atmospheric impurities preserved in glacial snow and ice.

3.6.1 Lead Isotope Systems

The concept of using lead isotopes as an environmental tracer is based on lead isotopic variations that exist in the Earth's crust as a result of the radioactive decay of uranium and thorium. These variations are dependent on the geological history and age of crustal regions. For lead ores, the isotopic composition has remained the same since mineral formation when the ore was geochemically separated from surrounding source rocks

containing uranium and thorium. There exist variations in isotopic composition of lead ore bodies as a result of the mixing of primordial lead and radiogenic lead in the surrounding source region, before the separation of the mineral from the surrounding system. The subsequent isotopic composition of an ore body and its geological age is then dependent on the time of this isolation.[4]

The relationship between the isotopic composition of terrestrial lead and its geological age can be illustrated using a radiogenic growth curve (Figure 3.9). The ages shown in the figure (in years before present, BP) indicate the isotopic composition of the ore body at the time of isolation from the source region.[4] Older lead ore bodies, for which the geochemical separation occurred billions of years ago, have an 'unradiogenic' isotopic composition with $^{206}Pb/^{207}Pb$ ratios as low as ~ 1. Younger lead ore bodies, for which geochemical separation occurred in more recent geological history, and crustal rocks, are characterised by a more 'radiogenic' isotopic composition, with $^{206}Pb/^{207}Pb$ ratios of ~ 1.20 and reaching as high as ~ 1.30.

Regional variations in lead isotopic composition that exist between different lead ore bodies, and between lead ore bodies and crustal material, allow different sources of lead to be distinguished. Assuming that the mineralogy and isotopic composition of atmospheric lead reflect the geographical location of its source area and is not substantially modified during transport,[206,207] the isotopic composition of lead measured in environmental samples, such as glacial snow and ice, can be used to trace the source region of the dust and therefore infer atmospheric transport patterns. These techniques have been successfully used to trace the sources of anthropogenic and natural impurities preserved in glacial snow and ice in regions such as Antarctica,[208–210] Greenland,[211] the Himalayas,[212] Bolivia,[213] and Europe,[214] and also the pollution of the oceans.[215]

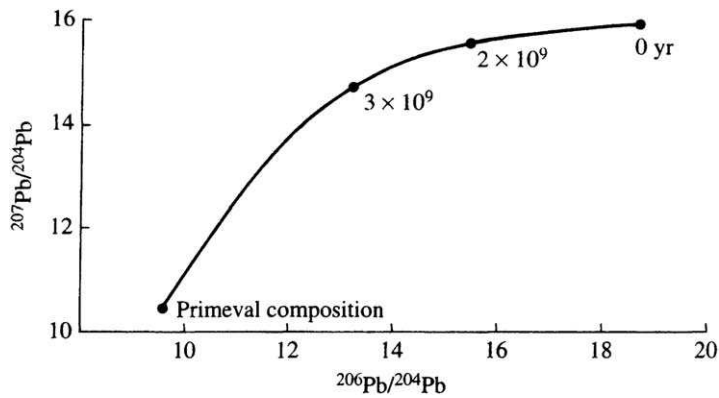

Figure 3.9 Common lead growth curve; ages are given in years before present (BP) Adapted from Figure 19.2 in Faure,[4] Copyright © 1977, 1986, by John Wiley & Sons, Inc.

3.7 Progress in Analytical Techniques

3.7.1 TIMS

Innovations in automation[216,217] and the release of commercially available TIMS instruments have brought about improvements in electronics, magnet and detector geometry, and ion optics. The advent of multiple collector geometries (multi-collection) together with the advent of low-noise high-stability electronics enabled simultaneous ion beam detection, thereby mitigating the effects of ion beam intensity fluctuations. As a result, analytical precision improved from the 0.1–0.01% range in the 1960s and 1970s (automation), over 0.1–0.01‰ in the 1980s and 1990s (magnet geometry, multi-collection), and into the 0.001‰ range since the early 2000s (ion optics, software-controlled movable Faraday cups). The advent of detectors with a uniform response, software-controlled amplifier–detector associations, and correction of the electronic drift of the amplifier resistors has pushed long-term reproducibility to the statistical counting limits.

Means to meet the analytical demands of the mass spectrometry community for lower levels of detection, without sacrificing precision and accuracy, include dynamic ranges spanning several orders of magnitude, ion-counting multi-collection systems, and minimisation of peak tailing effects. The ions per atom used is increasing steadily over time, currently reaching percent levels for most elements in MC-ICPMS instruments. Precision will ultimately be limited by the number of atoms present in the amount of sample processed for analysis and the relevant concentration of the element under investigation. Reducing the procedural blank accordingly is not a minor problem in this context.

3.7.2 New Generation of Noble Gas Mass Spectrometers

Perhaps the most important recent technical development of the ^{40}Ar–^{39}Ar technique is the availability of a new generation of noble gas mass spectrometers. Unlike the older instruments (*e.g.* MAP 215–50, VG5400) which require peak-hopping measurement of the five argon isotopes (^{40}Ar to ^{36}Ar) on a single multiplier, the new machines allow multi-collection in real time, by using a combination of Faraday cups and ion-counting multipliers. Whereas multi-collection using only multipliers is not yet beneficial to the ^{40}Ar–^{39}Ar technique because of the uncertainties associated with the multiplier calibrations, multi-collection using five Faraday cups or four Faraday cups and one ion-counting detector have shown that great improvements can be made to the analytical precision. In some case, an improvement in precision of one order of magnitude compared to the old machines has been measured, similar to the evolution of TIMS instruments. However, the most striking improvement to date concerns young volcanic rocks with large amount of trapped ^{40}Ar, where a precision improvement of $\sim$20-fold has been measured. Phillips[218] compared an age of 300 ± 60 ka obtained using a

VG5400 on a low-potassium tholeiitic volcanic rock (a type of rock particularly notorious for giving low-precision ^{40}Ar–^{39}Ar ages), with an age of 300 ± 2 ka when the same rock is ^{40}Ar–^{39}Ar dated using an ARGUS VI machine. At the time of writing, no data obtained with this new generation of machine have yet been published, particularly those using a combination of Faraday cups and multipliers, but it is obvious that these instruments will revolutionise the field of ^{40}Ar–^{39}Ar dating and when combined with the revision of the ^{40}K decay constants,[119] will provide data with a precision difficult to rival, particularly for the Phanerozoic timescale.

References

1. A. P. Dickin, *Radiogenic Isotope Geology*, Cambridge University Press, New York, 2nd edn, 2005.
2. C. J. Allègre, *Isotope Geology*, Cambridge University Press, New York, 2008.
3. G. Faure and T. M. Mensing, *Isotopes: Principles and Applications*, 2004.
4. G. Faure, in *Principles of Isotope Geology*, John Wiley & Sons, New York, 2nd edn, 1986, pp. 309–340.
5. J. J. Thomson, *Proc. R. Soc.*, 1913, **A 89**, 1.
6. A. J. Dempster, *Phys. Rev.*, 1918, **11**, 316.
7. F. W. Aston, *Philos. Mag. Series 6*, 1919, **38**, 707.
8. K. T. Bainbridge and E. B. Jordan, *Phys. Rev.*, 1936, **50**, 282.
9. A. O. Nier, *Rev. Sci. Instrum.*, 1940, **11**, 212.
10. J. R. de Laeter, *Applications of Inorganic Mass Spectrometry,* John Wiley & Sons, New York, 2001, pp. 3–18.
11. W. G. Cross, *Rev. Sci. Instrum.*, 1951, **22**, 717.
12. W. A. Chupka and M. G. Inghram, *J. Chem. Phys.*, 1953, **21**, 1313.
13. A. E. Cameron, D. H. Smith and R. L. Walker, *Anal. Chem.*, 1969, **41**, 525.
14. G. F. Kessinger and J. E. Delmore, *Int. J. Mass Spectrom.*, 2002, **213**, 63.
15. T. Miyazaki, T. Shibata, M. Yoshikawa, T. Sakamoto, K. Iijima and Y. Tatsumi, in *Frontier Research on Earth Evolution*, vol. 2, Institute for Frontier Research on Earth Evolution, Yokosuka, Japan, 2007, p. 1.
16. H. E. Duckworth, R. C. Barber and V. S. Venkatasubramanian, in *Mass Spectroscopy*, Cambridge University Press, Cambridge, 2nd edn, 1986, p. 42.
17. G. W. Lugmair and R. W. Carlson, *Proc. 9th Lunar and Planet. Sci. Conf.*, Houston, TX, 1978, pp. 689–704.
18. B. Jacobsen, Q.-Z. Yin, F. Moynier, Y. Amelin, A. N. Krot, K. Nagashima, I. D. Hutcheon and H. Palme, *Earth Planet. Sci. Lett.*, 2008, **272**, 353.
19. J. Villeneuve, M. Chaussidon and G. Libourel, *Science*, 2009, **325**, 985.
20. K. K. Larsen, A. Trinquier, C. Paton, M. Schiller, D. Wielandt, M. A. Ivanova, J. N. Connelly, A. Nordlund, A. N. Krot and M. Bizzarro, *Astrophys. J., Lett.*, 2011, **735**, L37.
21. N. T. Kita, T. Ushikubo, K. B. Knight, A. Ruslan, A. Mendybaev, A. M. Davis, F. M. Richter and J. H. Fournelle, *Geochim. Cosmochim. Acta*, 2012, **86**, 37.

22. G. J. Wasserburg, J. Wimpenny and Q.-Z. Yin, *Meteorit. Planet. Sci.*, 2012, **47**, 1980.
23. C. M. Gray and W. Compston, *Nature*, 1974, **251**, 495.
24. T. Lee, D. A. Papanastassiou and G. J. Wasserburg, *Astrophys. J., Lett.*, 1977, **211**, L107.
25. E. Kurahashi, N. T. Kita, H. Nagahara and Y. Morishita, *Geochim. Cosmochim. Acta*, 2008, **72**, 3865.
26. A. N. Krot, Y. Amelin, P. Bland, F. J. Ciesla, J. Connelly, A. M. Davis, G. R. Huss, I. D. Hutcheon, K. Makide, K. Nagashima, L. E. Nyquist, S. S. Russell, E. R. D. Scott, K. Thrane, H. Yurimoto and Q.-Z. Yin, *Geochim. Cosmochim. Acta*, 2009, **73**, 4963.
27. A. K. Kennedy, J. R. Beckett and I. D. Hutcheon, *Geochim. Cosmochim. Acta*, 1997, **61**, 1541.
28. C. Vockenhuber, F. Oberli, M. Bichler, I. Ahmad, G. Quitté, M. Meier, A. N. Halliday, D. C. Lee, W. Kutschera, P. Steier, R. J. Gehrke and R. G. Helmer, *Phys. Rev. Lett.*, 2004, **93**, 172501.
29. D. C. Lee and A. N. Halliday, *Nature*, 1995, **378**, 771.
30. C. L. Harper and S. B. Jacobsen, *Geochim. Cosmochim. Acta*, 1996, **60**, 1131.
31. M. F. Horan, M. I. Smoliar and R. J. Walker, *Geochim. Cosmochim. Acta*, 1998, **62**, 545.
32. M. J. Walter and Y. Thibault, *Science*, 1995, **270**, 1186.
33. M. J. Walter, H. E. Newsom, W. Ertel and A. Holzheid, in *Origin of the Earth and Moon*, ed. R. M. Canup and K. Righter, Lunar and Planetary Institute, Houston, TX, 2000.
34. T. Kleine, K. Mezger, H. Palme, E. Scherer and C. Münker, *Geochim. Cosmochim. Acta*, 2005, **69**, 5805.
35. A. Q. Markowski, G., A. N. Halliday and T. Kleine, *Earth Planet. Sci. Lett.*, 2006, **242**, 1.
36. A. Schérsten, T. Elliott, C. Hawkesworth, S. S. Russell and J. Masarik, *Earth Planet. Sci. Lett.*, 2006, **241**, 530.
37. L. P. Qin, N. Dauphas, M. Wadhwa, J. Masarik and P. E. Janney, *Earth Planet. Sci. Lett.*, 2008, **273**, 94.
38. T. S. Kruijer, P. Sprung, T. Kleine, I. Leya, C. Burkhardt and R. Wieler, *Geochim. Cosmochim. Acta*, 2012, **99**, 287.
39. T. Kleine, K. Mezger, C. Münker, H. Palme and A. Bischoff, *Geochim. Cosmochim. Acta*, 2004, **68**, 2935.
40. C. Burkhardt, T. Kleine, H. Palme, B. Bourdon, J. Zipfel, J. Friedrich and D. Ebel, *Geochim. Cosmochim. Acta*, 2008, **72**, 6177.
41. T. Kleine, C. Münker, K. Mezger and H. Palme, *Nature*, 2002, **418**, 952.
42. R. Schoenburg, B. S. Kamber, K. D. Collerson and O. Eugster, *Geochim. Cosmochim. Acta*, 2002, **66**, 3151.
43. Q.-Z. Yin, S. B. Jacobsen, K. Yamashita, J. Blichert-Toft, P. Télouk and F. Albarède, *Nature*, 2002, **418**, 949.
44. Lee, A. N. Halliday, G. A. Snyder and L. A. Taylor, *Science*, 1997, **278**, 1098.

45. C. N. Foley, M. Wadhwa, L. E. Borg, P. E. Janney, R. Hines and T. L. Grove, *Geochim. Cosmochim. Acta*, 2005, **69**, 4557.
46. N. Dauphas and A. Pourmand, *Nature*, 2011, **473**, 489.
47. R. J. Arevalo and W. F. McDonough, *Earth Planet. Sci. Lett.*, 2008, **272**, 656.
48. M. Touboul, T. Kleine, B. Bourdon, H. Palme and R. Wieler, *Nature*, 2007, **450**, 1206.
49. M. Touboul, T. Kleine, B. Bourdon, H. Palme and R. Wieler, *Icarus*, 2009, **199**, 245.
50. R. M. Canup, *Science*, 2012, **338**, 1052.
51. M. Ćuk and S. T. Stewart, *Science*, 2012, **338**, 1047.
52. K. Pahlevan and D. J. Stevenson, *Earth Planet. Sci. Lett.*, 2007, **262**, 438–449.
53. K. Righter and C. K. Shearer, *Geochim. Cosmochim. Acta*, 2003, **67**, 2497.
54. A. Corgne, C. Liebske, B. J. Wood, D. C. Rubie and D. J. Frost, *Geochim. Cosmochim. Acta*, 2005, **69**, 485.
55. A. D. Brandon, T. J. Lapen, V. Debaille, B. L. Beard, K. Rankenburg and C. Neal, *Geochim. Cosmochim. Acta*, 2009, **73**, 6421.
56. L. E. Borg, J. N. Connelly, M. Boyet and R. W. Carlson, *Nature*, 2011, **477**, 70.
57. A. Scherstén, T. Elliott, C. Hawkesworth and M. Norman, *Nature*, 2004, **427**, 234.
58. F. Moynier, Q.-Z. Yin, K. Irisawa, M. Boyet, B. Jacobsen and M. T. Rosing, *Proc. Natl Acad. Sci. U. S. A.*, 2010, **107**, 10810–10814.
59. T. Iizuka, S. Nakai, Y. V. Sahoo, A. Takamasa, T. Hirata and S. Maruyama, *Earth Planet. Sci. Lett.*, 2010, **291**, 189.
60. M. Touboul and R. J. Walker, *Int. J. Mass Spectrom.*, 2012, **309**, 109.
61. M. Willbold, T. Elliott and S. Moorbath, *Nature*, 2011, **477**, 195.
62. R. J. Walker, *Chem. Erde Geochem*, 2009, **69**, 101.
63. M. Touboul, I. S. Puchtel and R. J. Walker, *Science*, 2012, **335**, 1065.
64. V. S. Solomatov and C. C. Reece, *J. Geophys. Res.: Solid Earth*, 2008, **113**, B07408.
65. M. G. Jackson, R. W. Carlson, M. D. Kurz, P. M. Kempton, D. Francis and J. Bluszajn, *Nature*, 2008, **466**, 853.
66. T. Kleine, M. Touboul, J. A. Van Orman, B. Bourdon, C. Maden, K. Mezger and A. Halliday, *Earth Planet. Sci. Lett.*, 2008, **270**, 106.
67. M. Touboul, T. Kleine, B. Bourdon, J. A. Van Orman, C. Maden and J. Zipfel, *Earth Planet. Sci. Lett.*, 2009, **284**, 168.
68. T. Schulz, C. Münker, K. Mezger and H. Palme, *Geochim. Cosmochim. Acta*, 2010, **74**, 1706.
69. T. Schulz, D. Upadhyay, C. Münker and K. Mezger, *Geochim. Cosmochim. Acta*, 2012, **85**, 200.
70. T. Kleine, K. Mezger, H. Palme, E. Scherer and C. Münker, *Earth Planet. Sci. Lett.*, 2005, **231**, 41.
71. N. Kinoshita, M. Paul, Y. Kashiv, P. Collon, C. M. Deibel, B. DiGiovine, J. P. Greene, D. J. Henderson, C. L. Jiang, S. T. Marley, T. Nakanishi,

R. C. Pardo, K. E. Rehm, D. Robertson, R. Scott, C. Schmitt, 3. D. Tang, R. Vondrasek and A. Yokoyama, *Science*, 2012, **335**, 1614.
72. M. Boyet and R. W. Carlson, *Earth Planet. Sci. Lett.*, 2006, **250**, 254–268.
73. G. Caro, B. Bourdon, J. L. Birck and S. Moorbath, *Geochim. Cosmochim. Acta*, 2006, **70**, 164.
74. R. Andreasen, M. Sharma, K. V. Subbarao and S. G. Viladkar, *Earth Planet. Sci. Lett.*, 2008, **266**, 14.
75. D. T. Murphy, A. D. Brandon, V. Debaille, R. Burgess and C. J. Ballentine, *Geochim. Cosmochim. Acta*, 2010, **74**, 738.
76. A. Cipriani, E. Bonatti and R. W. Carlson, *Geochem. Geophys. Geosyst.*, 2011, **12**, 1.
77. M. G. Jackson and R. W. Carlson, *Geochem. Geophys. Geosyst.*, 2012, **13**.
78. M. Boyet, J. Blichert-Toft, M. Rosing, M. Storey, P. Télouk and F. Albarède, *Earth Planet. Sci. Lett.*, 2003, **214**, 427.
79. G. Caro, B. Bourdon, J.-L. Birck and S. Moorbath, *Nature*, 2003, **423**, 428.
80. C. L. Harper and S. B. Jacobsen, *Nature*, 1992, **360**, 728.
81. H. Rizo, M. Boyet, J. Blichert-Toft and M. Rosing, *Earth Planet. Sci. Lett.*, 2011, **312**, 267.
82. H. Rizo, M. Boyet, J. Blichert-Toft, J. O'Neil, M. Rosing and J.-L. Paquette, *Nature*, 2012, **491**, 96.
83. J. O'Neil, R. W. Carlson, D. Francis and R. K. Stevenson, *Science*, 2008, **321**, 1828.
84. J. O'Neil, R. W. Carlson, J. Paquette and D. Francis, *Precambrian Res.*, 2012, **220–221**, 23.
85. A. S. G. Roth, B. Bourdon, S. J. Mojzsis, M. Touboul, P. Sprung, M. Guitreau and J. Blichert-Toft, *Earth Planet. Sci. Lett.*, 2013, **361**, 50.
86. M. Boyet and R. W. Carlson, *Science*, 2005, **309**, 576.
87. G. Caro, B. Bourdon, A. N. Halliday and G. Quitté, *Nature*, 2008, **452**, 336.
88. R. Andreasen and M. Sharma, *Science*, 2006, **314**, 806.
89. R. W. Carlson, M. Boyet and M. F. Horan, *Science*, 2007, **316**, 1175.
90. A. Gannoun, M. Boyet, H. Rizo and A. El Goresy, *PNAS*, 2011, **108**, 7693.
91. D. A. Papanastassiou and G. J. Wasserburg, *Earth and Planetary Science Letters*, 1972, **13**, 368–374.
92. A. H. Jaffey, K. F. Flynn, L. E. Glendenin, W. C. Bentley and A. M. Essling, *Phys. Rev.*, 1971, **4**, 1889.
93. J. M. Mattinson, *Chem. Geol.*, 2010, **275**, 186.
94. B. Schoene, J. L. Crowley, D. J. Condon, M. D. Schmitz and S. A. Bowring, *Geochim. Cosmochim. Acta*, 2006, **70**, 426.
95. G. R. Tilton, C. Patterson, H. Brown, M. G. Inghram, R. Hayden, D. Hess and E. Larsen Jr, *Geol. Soc. Am. Bull.*, 1955, **66**, 1131.
96. G. R. Tilton, G. W. Wetherill, G. L. Davis and C. A. Hopson, *Geol. Soc. Am. Bull.*, 1958, **69**, 1469.
97. G. W. Wetherill, *Trans., Am. Geophys. Union*, 1956, **37**, 320.
98. W. Compston, I. S. Williams and C. Meyer, *J. Geophys. Res.*,**89**(S02), B525–B534.

99. R. Mundil, I. Metcalfe, K. R. Ludwig, P. R. Renne, F. Oberli and R. S. Nicoll, *Earth Planet. Sci. Lett.*, 2001, **187**, 131.
100. Lee, I. S. Williams and D. J. Ellis, *Nature*, 1997, **390**, 159.
101. A. Davidson and O. Breemen, *Contrib. Mineral. Petrol.*, 1988, **100**, 291.
102. Y. Amelin, A. Kaltenbach, T. Iizuka, C. H. Stirling, T. R. Ireland, M. Petaev and S. B. Jacobsen, *Earth Planet. Sci. Lett.*, 2010, **300**, 343.
103. I. R. Fletcher, B. Rasmussen and N. J. McNaughton, *Aust. J. Earth Sci.*, 2000, **48**, 845.
104. E. S. Schandl, D. W. Davis and T. E. Krogh, *Geology*, 1990, **18**, 505.
105. R. L. Romer and J. E. Wright, *Geochim. Cosmochim. Acta*, 1992, **56**, 2137.
106. R. R. Parrish, *Can. J. Earth Sci.*, 1990, **11**, 1431.
107. D. A. Richards, S. H. Bottrell, R. A. Cliff, K. Ströhle and P. J. Rowe, *Geochim. Cosmochim. Acta*, 1998, **62**, 3683.
108. J. Woodhead and R. Pickering, *Chem. Geol.*, 2012, **322**, 290.
109. S. A. Wilde, J. W. Valley, W. H. Peck and C. M. Graham, *Nature*, 2001, **409**, 175.
110. S. W. Denyszyn, R. Mundil, S. J. Brownlee and P. R. Renne, *Can. J. Earth Sci.*, 2011, **48**, 557.
111. S. L. Kamo, G. K. Czamanske, Y. Amelin, V. A. Fedorenko, D. W. Davis and V. R. Trofimov, *Earth Planet. Sci. Lett.*, 2003, **214**, 75.
112. R. Mundil, J. Pálfy, P. R. Renne and P. Brack, in *The Triassic Timescale*, Special Publication, Geological Society, London, 2010, **334**, 41.
113. J.-Y. Lee, K. Marti, J. P. Severinghaus, K. Kawamura, H.-S. Yoo, J. B. Lee and J. S. Kim, *Geochim. Cosmochim. Acta*, 2006, **70**, 4507.
114. I. McDougall and T. M. Harrison, *Geochronology and Thermochronology by the $^{40}Ar/39Ar$ method*, Oxford University Press, Oxford, 1999.
115. A. K. Baksi, in *The Origin of Melting Anomalies, Plates, Plumes and Planetary Processes*, ed. G. R. Foulger and D. M. Jurdy, Geological Society of America Special Paper, 2007, vol. **430**, pp. 285–304.
116. R. H. Steiger and E. Jäger, *Earth Planet. Sci. Lett.*, 1977, **36**, 359.
117. K. Min, R. Mundil, P. R. Renne and K. R. Ludwig, *Geochim. Cosmochim. Acta*, 2000, **64**, 73.
118. F. Jourdan, A. Marzoli, H. Bertrand, S. Cirille, L. Tanner, D. J. Kontak, G. McHone, P. R. Renne and G. Bellieni, *Lithos*, 2009, **110**, 167.
119. P. R. Renne, R. Mundil, G. Balco, K. Min and K. R. Ludwig, *Geochim. Cosmochim. Acta*, 2010, **74**, 5349.
120. P. R. Renne, W. D. Sharp, A. L. Deino, G. Orsi and L. Civetta, *Science*, 1997, **277**, 1279.
121. D. D. Bogard, *Meteoritics*, 1995, **30**, 244.
122. F. Jourdan, D. F. Mark and C. Verati, *Advances in $^{40}Ar/^{39}Ar$ Dating from Acheology to Planetary Sciences*, Special Publication, Geological Society, London, 2013.
123. G. Turner, J. C. Huneke, F. A. Podosek and W. G. J., *Earth Planet. Sci. Lett.*, 1971, **12**, 19.
124. F. Jourdan, *Aust. J. Earth Sci.*, 2012, **59**, 199.

125. T. Kennedy, F. Jourdan, A. W. R. Bevan and M. A. M. Gee, Frew, *Geochim. Cosmochim. Acta*, 2013, **115**, 162–182.
126. M. D. Norman, R. A. Duncan and J. J. Huard, *Geochim. Cosmochim. Acta*, 2006, **70**, 6032.
127. E. K. Jessberger, J. C. Hueneke, F. A. Podosek and G. Wasserburg, *Proc. 5th Lunar Sci. Conf.*, Pergamon, New York, 1974, pp. 1419–1449.
128. T. S. Culler, T. A. Becker, M. R. A. and P. R. Renne, *Science*, 2000, **287**, 1785.
129. N. E. B. Zellner, J. W. Delano, T. D. Swindle, F. Barra, E. Olsen and D. C. B. Whittet, *Geochim. Cosmochim. Acta*, 2009, **73**, 4590.
130. S. Hui, M. Norman and F. Jourdan, *Proc. 7th Australian Space Sci. Conf.*, Sydney, 2010.
131. B. A. Cohen, G. A. Snyder, C. M. Hall, L. A. Taylor and M. A. Nazarov, *Meteorit. Planet. Sci.*, 2001, **36**, 1345.
132. M. Trieloff, E. K. Jessberger, I. Herrwerth, J. Hopp, C. Fleni, M. Ghells, M. Bourot-Denise and P. Pellas, *Nature*, 2003, **422**, 502.
133. S. M. Aciego, F. Jourdan, D. J. DePaolo, M. Kennedy, P. R. Renne and K. W. W. Sims, *Geochem. Geophys. Geosyst.*, 2010, **74**, 1620.
134. A. Hicks, J. Barclay, D. F. Mark and S. Loughlin, *Geology*, 2012, **40**, 723.
135. W. D. Sharp and P. R. Renne, *Geochem. Geophys. Geosyst.*, 2005, **6**.
136. C. Hofmann, G. Feraud and V. Courtillot, *Earth Planet. Sci. Lett.*, 2000, **180**, 13.
137. C. Verati and F. Jourdan, in *$^{40}Ar/^{39}Ar$ Dating: From Geochronology to Thermochronology, from Archaeology to Planetary Sciences*, ed. F. Jourdan, D. Mark and C. Verati, Special Publication 378, Geological Society, London, 2014.
138. A. Marzoli, P. R. Renne, E. M. Piccirillo, M. Ernesto, G. Bellieni and A. De Min, *Science*, 1999, **284**, 616.
139. M. K. Reichow, A. D. Saunders, R. V. White, M. S. Pringle, A. I. Al'Mukhamedov, A. I. Medvedev and N. P. Kirda, *Science*, 2002, **296**, 1846.
140. F. Jourdan, G. Féraud, H. Bertrand, M. K. Watkeys and P. R. Renne, *Geochem. Geophys. Geosyst.*, 2008, **9**.
141. C. Cucciniello, L. Melluso, F. Jourdan, J. J. Mahoney, T. Meisel and V. Morra, *Geol. Mag.*, 2013, **150**, 1.
142. V. E. Courtillot and P. R. Renne, *C. R. Geosci*, 2003, **335**, 113–140.
143. M. Storey, R. G. Roberts and M. Saidin, *Proc. Natl. Acad. Sci. U. S. A.*, 2012, **109**, 18684.
144. R. C. Walter, *Geology*, 1994, **22**, 6.
145. B. Carrapa, J. Wijbrans and G. Bertotti, *Geology*, 2003, **31**, 601.
146. G. Sanchez, Y. Rolland, J. Schneider, M. Corsini, E. Oliot, P. Goncalves, C. Verati, J. M. Lardeaux and D. Marquer, *Lithos*, 2011, **125**, 521.
147. C. Wobus, M. Pringle, K. Whipple and K. Hodges, *Earth Planet. Sci. Lett.*, 2008, **269**, 1.
148. C. J. Forbes, D. Giles, F. Jourdan, K. Sato, S. Omori and M. Bunch, *Precambrian Res.*, 2012, **200–203**, 209.

149. K. Ueda, J. Jacobs, R. J. Thomas, J. Kosler, M. S. A. Horstwood, J.-A. Wartho, F. Jourdan, B. Emmel and R. Matola, *J. Geol.*, 2012, **120**, 507.
150. O. Oliveros, D. Tristá-Aguilera, G. Féraud, D. Morata, L. Aguirre, S. Kojima and F. Ferraris, *Miner. Deposita*, 2008, **43**, 61.
151. I. Márton, R. Moritz and R. Spikings, *Tectonophysics*, 2010, **483**, 240.
152. Q. Zeng, T. C. McCuaig, C. J. R. Hart, F. Jourdan, J. Muhling and L. Bagas, *Miner. Deposita*, 2012, **47**, 799.
153. R.-Z. Hu, W.-F. Wei, 3.-W. Bi, J.-T. Peng, Y.-Q. Qi, L.-Y. Wu and Y.-W. Chen, *Lithos*, 2012, **150**, 111.
154. J. D. Vervoot and J. Blichert-Toft, *Geochim. Cosmochim. Acta*, 1999, **63**, 553.
155. J. D. Vervoot, D. Jeff, P. J. Patchett, J. Blichert-Toft and F. Albarède, *Earth Planet. Sci. Lett.*, 1999, **168**, 79.
156. A. L. S. Kemp, C. J. Hawkesworth, B. Paterson and P. Kinny, *Nature*, 2006, **439**, 580.
157. C. J. Hawkesworth and A. L. S. Kemp, *Chem. Geol.*, 2006, **226**, 144.
158. E. Belousova, W. L. Griffin and S. Y. O'Reilly, *J. Petrol.*, 2006, **47**, 329.
159. A. L. S. Kemp, C. J. Hawkesworth, G. L. Foster, B. A. Paterson, J. D. Woodhead, J. M. Hergt, C. M. Gray and M. J. Whitehouse, *Science*, 2007, **315**, 980.
160. K. C. Condie, E. Beyer, E. Belousova, W. L. Griffin and S. Y. O'Reilly, *Precambrian Res.*, 2005, **139**, 42.
161. W. L. Griffin, N. J. Pearson, E. A. Belousova, S. R. Jackson, E. van Achterbergh, S. Y. O'Reilly and S. R. Shee, *Geochim. Cosmochim. Acta*, 2000, **64**, 133.
162. W. L. Griffin, E. Belousova, S. G. Walters and S. Y. O'Reilly, *Aust. J. Earth Sci.*, 2006, **53**, 125.
163. P. J. Patchett, O. Kouvo, C. E. Hedge and M. Tatsumoto, *Contrib. Mineral. Petrol.*, 1981, **78**, 279.
164. P. E. Smith, M. Tatsumoto and R. Farquhar, *Contrib. Mineral. Petrol.*, 1987, **97**, 93.
165. E. Scherer, C. Muenker and K. Mezger, *Science*, 2001, **293**, 683.
166. E. Belousova, Y. A. Kostitsyn, W. L. Griffin, G. C. Begg, S. Y. O'Reilly and N. J. Pearson, *Lithos*, 2010, **119**, 457.
167. W. J. Collins, E. A. Belousova, A. L. S. Kemp and J. B. Murphy, *Nat. Geosci.*, 2011, **4**, 333.
168. S. B. Shirey and R. J. Walker, *Annu. Rev. Earth Planet. Sci.*, 1998, **26**, 423–500.
169. L. Reisberg and T. Meisel, *Geostand. Newsl.*, 2002, **26**, 249–267.
170. R. W. Carlson, *Lithos*, 2005, **82**, 249–272.
171. R. W. Carlson, S. B. Shirey and M. Schonbachler, *Elements*, 2008, **4**, 239–245.
172. R. J. Walker, J. W. Morgan, E. S. Beary, M. I. Smoliar, G. K. Czamanske and M. F. Horan, *Geochim. Cosmochim. Acta*, 1997, **61**, 4799–4807.
173. I. S. Puchtel, R. J. Walker, C. R. Anhaeusser and G. Gruau, *Chem. Geol.*, 2009, **262**, 355–369.

174. I. S. Puchtel, R. J. Walker, A. D. Brandon and E. G. Nisbet, *Geochim. Cosmochim. Acta*, 2009, **73**, 6367–6389.
175. B. D. Connolly, I. S. Puchtel, R. J. Walker, R. J. Arevalo, P. M. Piccoli, G. R. Byerly, C. Robin-Popieul and N. T. Arndt, *Earth Planet. Sci. Lett.*, 2011, **311**, 253–263.
176. H. J. Stein, R. J. Markey, J. W. Morgan, J. L. Hannah and A. Schersten, *Terr. Nova*, 2001, **13**, 479–486.
177. T. E. McCandless, J. Ruiz, B. I. Adair and C. Freydier, *Geochim. Cosmochim. Acta*, 1999, **63**, 911–923.
178. R. J. Walker, H. M. Prichard, A. Ishivatari and M. Pimentel, *Geochim. Cosmochim. Acta*, 2002, **66**, 329–345.
179. I. S. Puchtel, G. E. Brügmann, A. W. Hofmann, V. S. Kulikov and V. V. Kulikova, *Contrib. Mineral. Petrol.*, 2001, **140**, 588–599.
180. R. J. Walker, J. W. Morgan, A. J. Naldrett, C. Li and J. D. Fassett, *Earth Planet. Sci. Lett.*, 1991, **105**, 416–429.
181. R. J. Walker, J. W. Morgan, E. J. Hanski and V. F. Smolkin, *Ontario Geol. Surv. Spec. Publ.*, 1994, **5**, 343–355.
182. J. Kirk, J. Ruiz, J. Chesley, J. Walshe and G. England, *Science*, 2002, **297**, 1856–1858.
183. K. J. Westerlund, S. B. Shirey, S. H. Richardson, R. W. Carlson, J. J. Gurney and J. W. Harris, *Contrib. Mineral. Petrol.*, 2006, **152**, 275–294.
184. A. S. Cohen, A. L. Coe, J. M. Bartlett and C. J. Hawkesworth, *Earth Planet. Sci. Lett.*, 1999, **167**, 159–173.
185. D. Selby and R. A. Creaser, *Science*, 2005, **308**, 1293–1295.
186. D. Selby, R. A. Creaser and M. G. Fowler, *Geochim. Cosmochim. Acta*, 2007, **71**, 378.
187. A. J. Finlay, D. Selby and M. J. Osborne, *Earth Planet. Sci. Lett.*, 2012, **313–314**, 95.
188. A. J. Finlay, D. Selby, M. J. Osborne and D. Finucane, *Geology*, 2010, **38**, 979.
189. D. Rooney, D. Selby, M. D. Lewan, P. G. Lillis and J.-P. Houzay, *Geochim. Cosmochim. Acta*, 2012, **77**, 275.
190. D. Selby, R. A. Creaser, K. Dewing and M. Fowler, *Earth Planet. Sci. Lett.*, 2005, **235**, 1.
191. D. Selby and R. A. Creaser, *Science*, 2005, **308**, 1293.
192. R. J. Walker, R. W. Carlson, S. B. Shirey and F. R. Boyd, *Geochim. Cosmochim. Acta*, 1989, **53**, 1583–1595.
193. E. H. Hauri and S. R. Hart, *Chem. Geol.*, 1997, **139**, 185–205.
194. J. C. Lassiter and E. H. Hauri, *Earth Planet. Sci. Lett.*, 1998, **164**, 483–496.
195. J. C. Lassiter, E. H. Hauri, P. W. Reiners and M. O. Garcia, *Earth Planet. Sci. Lett.*, 2000, **178**, 269–284.
196. R. J. Walker, L. M. Echeverria, S. B. Shirey and M. F. Horan, *Contrib. Mineral. Petrol.*, 1991, **107**, 150–162.
197. A. D. Brandon, R. J. Walker, J. W. Morgan, M. D. Norman and H. M. Prichard, *Science*, 1998, **280**, 1570–1573.

198. I. S. Puchtel, A. D. Brandon, M. Humayun and R. J. Walker, *Earth Planet. Sci. Lett.*, 2005, **237**, 118–134.
199. J. W. Morgan, G. A. Wanderless, R. K. Petrie and A. J. Irving, *Tectonophysics*, 1981, **75**, 47–67.
200. J. W. Morgan, *Nature*, 1985, **317**, 703–705.
201. C.-L. Chou, D. M. Shaw and J. H. Crocket, *J. Geophys. Res.*, 1983, **88**, A507-A518.
202. M. D. Norman, V. C. Bennett and G. Ryder, *Earth Planet. Sci. Lett.*, 2002, **202**, 217–228.
203. I. S. Puchtel, R. J. Walker, O. B. James and D. A. Kring, *Geochim. Cosmochim. Acta*, 2008, **72**, 3022–3042.
204. M. Fischer-Gödde and H. Becker, *Geochim. Cosmochim. Acta*, 2012, **77**, 135–156.
205. F. E. Grousset and P. E. Biscaye, *Chem. Geol.*, 2005, **222**, 149.
206. H. Maring, D. M. Settle, P. Buat-Ménard, F. Dulac and C. C. Patterson, *Nature*, 1987, **300**, 154.
207. W. T. Sturges and L. A. Barrie, *Nature*, 1987, **329**, 144.
208. P. Vallelonga, K. Van de Velde, J. P. Candelone, V. I. Morgan, C. F. Boutron and K. J. R. Rosman, *Earth Planet. Sci. Lett.*, 2002, **204**, 291.
209. P. Vallelonga, P. Gabrielli, K. J. R. Rosman, C. Barbante and C. F. Boutron, *Geophys. Res. Lett.*, 2005, **32**, L01706.01701.
210. L. J. Burn-Nunes, P. Vallelonga, R. D. Loss, G. R. Burton, A. Moy, M. Curran, S. Hong, A. M. Smith, R. Edwards, V. I. Morgan and K. J. R. Rosman, *Geochim. Cosmochim. Acta*, 2011, **75**, 1.
211. G. R. Burton, J.-P. Candelone, K. J. R. Rosman, L. J. Burn, C. F. Boutron and S. Hong, *Earth Planet. Sci. Lett.*, 2007, **259**, 557.
212. K. Lee, S. D. Hur, S. Hou, L. J. Burn-Nunes, S. Hong, C. Barbante, C. F. Boutron and K. J. R. Rosman, *Sci. Total Environ.*, 2011, **412–413**, 194.
213. K. J. R. Rosman, S. Hong, G. R. Burton, L. J. Burn, C. F. Boutron, C. P. Ferrari, L. G. Thompson, L. Maurice-Bourgoin and B. Francou, *J. Phys. France IV*, 2003, **107**, 1157.
214. K. J. R. Rosman, C. V. Ly, K. P. Van de Velde and C. F. Boutron, *Earth Planet. Sci. Lett.*, 2000, **176**, 413.
215. R. M. Sherrell, E. A. Boyle and B. Hamelin, *J. Geophys. Res.*, 1992, **97**, 11257–11268.
216. W. Compston and P. A. Arriens, *Can. J. Earth Sci.*, 1968, **5**, 561.
217. G. J. Wasserburg, D. A. Papanastassiou, E. V. Nenow and C. A. Bauman, *Rev. Sci. Instrum.*, 1969, **40**, 288.
218. D. Phillips, in *34th IGC Conference*, Brisbane, 2012.